ISPRS Journal of Photogrammetry and Remote Sensing 210 (2024) 198–211

Contents lists available at ScienceDirect

ISPRS Journal of Photogrammetry and Remote Sensing

journal homepage: www.elsevier.com/locate/isprsjprs

A novel algorithm for ocean chlorophyll-*a* concentration using MODIS Aqua data

Julian Merder [a,*], Gang Zhao [a,1], Nima Pahlevan [b,c], Robert A. Rigby [d], Dimitrios M. Stasinopoulos [d], Anna M. Michalak [a]

[a] Department of Global Ecology, Carnegie Institution for Science, Stanford, CA, USA
[b] NASA Goddard Space Flight Center, Greenbelt, MD, USA
[c] Science Systems and Applications, Inc. (SSAI), Lanham, MD, USA
[d] School of Computing and Mathematical Sciences, University of Greenwich, UK

ARTICLE INFO

Keywords:
Chlorophyll-a Algorithm
MODIS Aqua
Ocean Color
GAMLSS
Chlorophyll-a Uncertainty
Water Quality Thresholds

ABSTRACT

The ability to infer ocean chlorophyll-*a* concentrations (Chl*a*) from spaceborne instruments is key to assessments of global ocean productivity and monitoring of water quality. Here, we present a novel parametric algorithm, OCG, trained on a set of global *in situ* high-performance liquid chromatography (HPLC) data that leverages Level-3 remote sensing reflectance (R_{rs}) products from the Moderate Resolution Imaging Spectroradiometer (MODIS) aboard the Aqua satellite. The OCG algorithm leverages more bands than existing algorithms and also provides pixel-wise uncertainty assessments that enable the calculation of the probability of exceeding specific Chl*a* thresholds. This feature has significant implications for water quality management, particularly in monitoring harmful algal blooms. The OCG surpasses existing algorithms in bias and accuracy without overfitting, especially in coastal areas, where it outperforms the current standard product (CI OC3) by 20 % in median symmetric accuracy. Moreover, the OCG reduces the signed symmetric percentage bias (SSPB) in coastal regions from 41 % (CI OC3) to below 5 %. Globally, the OCG algorithm yields lower Chl*a* in coastal regions, the Southern Ocean and the Mediterranean Sea, and higher values in the open ocean, particularly in ocean gyres and polar regions. For the Chesapeake Bay and the Baltic Sea, for example, daily OCG estimates for 2002 to 2021 are, on average, 2.9 g/L and 3.7 g/L lower than CI OC3 estimates, respectively. The presented approach also shows great potential for other existing and upcoming sensors, enabling widespread application in remote sensing.

1. Introduction

Phytoplankton represents the foundation of oceanic food webs and is responsible for nearly half of the net primary production on Earth (Field et al., 1998). It shapes nutrient cycles and is the motor of the biological carbon pump (Volk and Hoffert, 1985) by transferring organic carbon from the surface to the deep ocean, thus highly influencing the global carbon balance (Brewin et al., 2021; Falkowski et al., 1998). Chlorophyll-*a* represents the predominant photosynthetic pigment in phytoplankton (Björn et al., 2009). As a proxy for phytoplankton abundance and ocean color (Huot et al., 2007; O'Reilly et al., 1998), monitoring of the chlorophyll-*a* concentration (Chl*a*) builds the empirical basis required for understanding past, present, and future phytoplankton variability, eutrophication status, and water quality. Because of its critical role in the characterization of Earth's climate, Chl*a* is one of the essential climate variables as identified by the Global Climate Observing System and, as such, provides critical input to the United Nations Framework Convention on Climate Change (Bojinski et al., 2014; Hollmann et al., 2013).

The use of satellite remote sensing is currently the only way to view the entire surface ocean and to monitor Chl*a* at high temporal and spatial resolutions (Brewin et al., 2021). To enable such analyses, the remote sensing community has historically employed two algorithmic approaches to derive Chl*a*, namely empirical algorithms (Dierssen, 2010) and semi-analytical algorithms (IOCCG, 2006). Empirical algorithms, often referred to as ocean color algorithms (OC), make use of the

* Corresponding author.
E-mail address: jmerder@carnegiescience.edu (J. Merder).
[1] Present address: Key Laboratory of Water Cycle and Related Land Surface Processes, Institute of Geographic Sciences and Natural Resources Research, Chinese Academy of Sciences, Beijing, China.

https://doi.org/10.1016/j.isprsjprs.2024.03.014
Received 1 September 2023; Received in revised form 26 February 2024; Accepted 18 March 2024

special absorption properties of chlorophyll-*a* and use the satellite-derived water-leaving radiance or remote sensing reflectance (R_{rs}) to estimate Chl*a* from space (O'Reilly et al., 1998; O'Reilly and Werdell, 2019). These algorithms typically use the ratio of blue to green R_{rs} bands as explanatory variables (Groom et al., 2019; O'Reilly and Werdell, 2019) to leverage maximum and minimum absorption of chlorophyll-*a* in these spectral regions, respectively. Rather than solely relying on observed data, semi-analytical algorithms incorporate physical models (i.e., radiative transfer models) of light interaction with water constituents to estimate Chl*a* (IOCCG, 2006; Werdell et al., 2018). By incorporating these physical principles, semi-analytical algorithms provide a more mechanistic understanding of the processes influencing the observed remote sensing signal. However, as semi-analytical algorithms are often difficult to parametrize, empirical algorithms have been shown to usually outperform semi-analytical algorithms (Brewin et al., 2015b).

Current empirical OC algorithms, however, are also reported to exhibit biases over large-scale regions such as the Mediterranean Sea and the Southern Ocean (Bélanger et al., 2007; Volpe et al., 2007; Zeng et al., 2016). Moreover, because the standard OC algorithms are optimized for the open ocean, they show clear degradation in performance in coastal areas (IOCCG, 2000) where they are known to overestimate concentrations (Darecki and Stramski, 2004; McKee et al., 2007; Novoa et al., 2012; Tzortziou et al., 2007; Werdell et al., 2009). Although coastal shelves only represent about 7 % of the ocean surface, they contribute 10–30 % to the global primary production (Bauer et al., 2013) that, in turn, supports over 90 % of the global fish catch (Pauly et al., 2002). Coastal areas play a highly dynamic and essential role in the global carbon budget and can be either net carbon sources or sinks (Bauer et al., 2013). Reasons for biased Chl*a* estimates are high concentrations of suspended inorganic particles and colored dissolved organic matter as well as bathymetry, all of which add to the optical properties of such systems that are classified as Case 2 waters (IOCCG, 2000).

To improve the performance of the OC algorithms, regional, specialized, or adjusted algorithms have been developed. The most prominent one is the Color Index (Hu et al., 2012), which exhibits improved performance in the open ocean or more specifically at low Chl*a*. For this reason, the NASA Ocean Biology Processing Group blended the Color Index with OC algorithms at low Chl*a* concentrations (Hu et al., 2019; O'Reilly and Werdell, 2019) to create the currently employed NASA Chl*a* products (https://oceancolor.gsfc.nasa.gov/atbd/chlor_a/). Overestimations at high Chl*a* and Case 2 waters, however, remain unaffected. Algorithms optimized for those conditions, which often go beyond the blue and green band ratio by incorporating information from other R_{rs} bands, show improved performance in Case 2 waters or specific geographic regions (Al Shehhi et al., 2017; Brewin et al., 2015a; Darecki and Stramski, 2004; Gitelson et al., 2008; Gohin et al., 2002; Son and Kim, 2018), but cannot be used for the open ocean without a reparameterization (Cui et al., 2014; McKee et al., 2007). Another approach to improve performance has been to merge data and Chl*a* estimates from different satellites or sensors (Brewin et al., 2014; IOCCG, 2007). Although such approaches greatly improve the spatio-temporal coverage of Chl*a*, they introduce inter-sensor inconsistencies (Hammond et al., 2018) and are not guaranteed to remove observed biases or to yield improved estimates relative to single-sensor products (Moradi, 2021). In recent years, machine-learning approaches have also become widespread within the remote sensing community (Han et al., 2023) in an effort to improve the performance of Chl*a* estimates from remote sensing (Hieronymi et al., 2017; Ioannou et al., 2013; Pahlevan et al., 2020; Smith et al., 2021), but results from such models are often difficult to interpret and reproduce (Rudin, 2019). A simple, parametric empirical algorithm that performs well in both the open ocean and coastal waters globally is thus still missing.

In addition, the quantification of the uncertainty associated with Chl*a* estimates is also a highly desirable feature for ocean color products (Dierssen, 2010; Henson et al., 2010; IOCCG, 2019) for a variety of applications. Previous approaches to quantify estimation uncertainty have tried to classify Chl*a* uncertainty into uncertainty clusters or global uncertainty regions (Liu et al., 2021; Moore et al., 2009), to assess uncertainty by merging multiple Chl*a* estimates from different satellite sensors (Melin, 2010; Mélin et al., 2016), or to derive uncertainty metrics from neural networks (Saranathan et al., 2023; Werther et al., 2022a). A straightforward, robust, and parametric approach for quantifying the uncertainty of Chl*a* estimates from a single set of R_{rs} observations, however, is also still missing.

This study aims to develop a new, easily accessible, and transparent (i.e., parametric) empirical algorithm to improve Chl*a* estimates for both coastal and open ocean waters and to provide estimates of the Chl*a* uncertainty. To achieve this, we use **G**eneralized **A**dditive **M**odels for **L**ocation **S**cale and **S**hape (GAMLSS) (Rigby and Stasinopoulos, 2005; Stasinopoulos and Rigby, 2007), which is a distributional regression (Rigby and Stasinopoulos, 2005) that estimates the full conditional distribution of Chl*a*. This makes it possible to obtain pixel-wise uncertainty estimates and can also be used to gauge the magnitude of Chl*a* extremes or to calculate exceedance probabilities for Chl*a* thresholds. The latter is commonly used to track eutrophication status and assess the risk of harmful algal blooms (Gokul et al., 2019; Kress et al., 2019; Topcu and Brockmann, 2021) making the GAMLSS approach ideal for coastal water quality management, even in cases where specific Chl*a* thresholds vary between countries, regions or along salinity gradients (Maciel et al., 2022; Topcu and Brockmann, 2021; Williams et al., 2009).

The development of the new algorithm, named OCG (Ocean-Color-GAMLSS), is based on Level-3 Mapped R_{rs} imagery (NASA Goddard Space Flight Center, Ocean Ecology Laboratory, Ocean Biology Processing Group, 2018) from the Moderate Resolution Imaging Spectroradiometer (MODIS) on board of the Aqua satellite (Esaias et al., 1998). We compare the performance of the OCG to state-of-the-art OC algorithms, with a particular focus on the Color Index corrected OC3 (CI OC3) (Hu et al., 2019, 2012; O'Reilly and Werdell, 2019), which represents the current NASA standard product for MODIS Aqua. We then apply the OCG algorithm globally to illustrate the differences in Chl*a* relative to the CI OC3 algorithm across various geographic regions.

2. Data

In general, two types of variables are required to train empirical algorithms. One is a set of measured explanatory or independent variables, in this case, Level-3 R_{rs} spectral bands, while the other is the dependent variable, in this case *in situ* Chl*a*.

In contrast to classical OC algorithms, we performed model training on satellite-derived R_{rs} values (satellite matchups) instead of *in situ* R_{rs} values because by pairing satellite-derived R_{rs} with *in situ* measured Chl*a*, the impacts of uncertainty from both sensor calibration and atmospheric correction are collectively accounted for (Hu et al., 2013; Smith et al., 2021). The satellite matchup datasets were constructed by pairing *in situ* measured Chl*a* with the MODIS Aqua Level-3 Mapped R_{rs} imagery (NASA Goddard Space Flight Center, Ocean Ecology Laboratory, Ocean Biology Processing Group, 2018) from July 2002 to December 2021. Specifically, for each *in situ* location we searched for the overlapping pixel at 2.5 arcminute resolution (approximately 4.64 × 4.64 km at the equator) on the same calendar day and extracted data for all ten R_{rs} bands in the visible spectrum, i.e., $R_{rs}(412)$, $R_{rs}(443)$, $R_{rs}(469)$, $R_{rs}(488)$, $R_{rs}(531)$, $R_{rs}(547)$, $R_{rs}(555)$, $R_{rs}(645)$, $R_{rs}(667)$, $R_{rs}(678)$.

Level-3 satellite data has several benefits, such as the inclusion of high-quality products that pass a set of quality-control steps as part of standard NASA Level-3 products mapped onto a geo-referenced Earth grid (Scott and Werdell, 2019). Previous studies using Level-2 data often used a ~ 4.64 × 4.64 km pixel box centered on the *in situ* observation locations to extract satellite spectral information using a time window of three hours (Savtchenko et al., 2004; Seegers et al., 2018), but such a short time window limits the number of observations available for

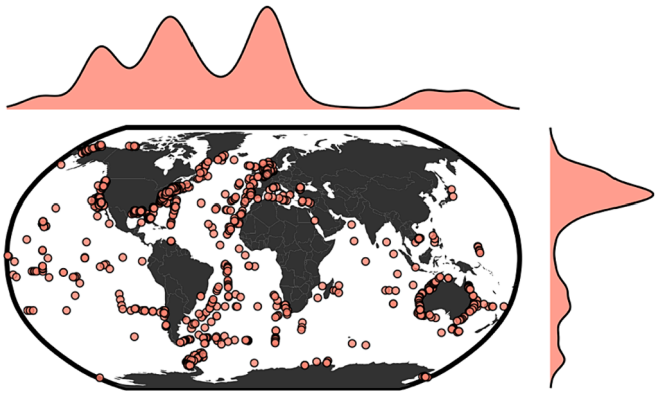

Fig. 1. Spatial distribution of satellite matchups with *in situ* HPLC Chl*a* observations used to train the OCG model. The marginal densities of points are presented at the top and right.

training. Although Level-3 data has a wider temporal window between the time of *in situ* measurement and the time of the satellite observation, the performance metrics applied to Level-3 data have been shown to remain comparable to Level-2 data (Scott and Werdell, 2019). The spatial and temporal mismatch between *in situ* Chl*a* observations and remote sensing information affects both Level-2 and Level-3 data and represents a source of uncertainty, as does the uncertainty of the R_{rs} values themselves. While these sources of uncertainty are not characterized directly here, they contribute to the overall GAMLSS model uncertainty to be investigated in future studies.

The *in situ* Chl*a* data used here are a compilation of multiple vessel surveys and databases assembled for the validation of ocean color algorithm estimates (Valente et al., 2019) and include global *in situ* Chl*a* values measured by both high-performance liquid chromatography (HPLC) and fluorometric and spectrophotometric methods. A detailed description of the data can be found in Valente et al. (2019). We used only HPLC data for model fitting because their accuracy is superior to fluorometric or spectrophotometric methods (Pinckney et al., 1994). Satellite matchups led to 2069 available *in situ* HPLC Chl*a* measurements (Fig. 1) for model fitting. However, we also considered the 5033 fluorometric and spectrophotometric satellite matchups in an additional algorithm evaluation (Supplementary Figure 1). For the latter set, we only used the data points where no simultaneous HPLC measurement exists to retain an independent dataset.

We compared the new OCG algorithm to the current state-of-the-art CI OC3 algorithm globally. The data used for this comparison represents global R_{rs} data assembled with the same resolution as in the model training, spanning daily estimates within the period of July 2002 to December 2021. Locations with no band information were excluded.

3. Description of the OCG algorithm

3.1. Existing OC algorithms

Classical OC algorithms assume that Chl*a* has a conditional lognormal distribution (O'Reilly and Werdell, 2019). This means that models are trained on log-transformed (base 10) *in situ* measured Chl*a*, and the conditional distribution of log Chl*a* is then normally distributed with a mean (μ), which is a function of explanatory variables, and a fixed standard deviation (σ). Existing OC algorithms use a 4th-order polynomial of a logarithmized (base 10) ratio between blue and green R_{rs} bands to represent μ (O'Reilly and Werdell, 2019). More specifically, the numerator is the maximum of the bands $R_{rs}(443)$ and $R_{rs}(488)$ for the OC3 algorithm, and the denominator $R_{rs}(547)$. For OC2, the numerator is based on $R_{rs}(488)$ only. Hence, the OC2 and OC3 algorithms use a quartic polynomial with a single explanatory variable but this single term involves two or three bands, respectively. The back transformation of OC models to the original Chl*a* scale is done by calculating ten to the power of μ, and as such the estimates represent the median Chl*a* estimate rather than its mean (Campbell, 1995). Those median Chl*a* estimates are then merged with the Color Index as this has been found to improve the performance of OC algorithms for low Chl*a* (Hu et al., 2012). The Color Index corrected OC algorithms (e.g., CI OC3) use the Color Index estimate (Hu et al., 2019, 2012) when Chl*a* of the Color Index estimate falls below 0.25 ug/L and uses the weighted average between the Color Index and respective OC estimate between 0.25 and 0.35 ug/L. At Color Index estimates above 0.35 ug/L the estimate of the OC algorithm is used (https://oceancolor.gsfc.nasa.gov/atbd/chlor_a/). Other thresholds for blending have been employed in the past (Hu et al., 2019; O'Reilly and Werdell, 2019). The CI OC3 algorithm is the current standard algorithm for MODIS Aqua (O'Reilly and Werdell, 2019, https://oceancolor.gsfc.nasa.gov/atbd/chlor_a/).

By modeling only μ but keeping σ constant, OC algorithms as well as machine learning algorithms such as (Bayesian) neural networks (O'Reilly and Werdell, 2019; Saranathan et al., 2023; Werther et al., 2022a) leave out important properties of the underlying data. This is because σ can also depend on the values of R_{rs} bands themselves. Moreover, R_{rs} bands may also impact the skewness and kurtosis of a distribution. This has not only an impact on model performance (Stasinopoulos and Rigby, 2007) but direct implications for the creation of uncertainty estimates, which is currently ignored (Saranathan et al., 2023; Werther et al., 2022a; Werther et al., 2022b).

3.2. GAMLSS approach for estimating uncertainty, quantiles, and exceedance probabilities

Unlike existing approaches, the OCG algorithm is based on the GAMLSS approach, which is a distributional regression that models all parameters of a distribution as functions of explanatory variables (Rigby and Stasinopoulos, 2005; Stasinopoulos et al., 2017). GAMLSS models are fitted using the "gamlss" package and relevant add-ons for visualization of results in "R" (Stasinopoulos and Rigby, 2007; Stasinopoulos et al., 2022). Characterization of the conditional distribution of Chl*a* makes it possible to estimate potential Chl*a* extreme event magnitudes (e.g., the 0.95 quantile) or the exceedance probability of water-quality-relevant Chl*a* thresholds. The principle is illustrated in Fig. 2a.

Moreover, the estimated conditional distribution of Chl*a* can be used to produce pixel-wise uncertainty estimates. Pixel-wise uncertainty can be specified in many ways, such as the quartile coefficient of dispersion, which is calculated as the interquartile range (the 0.75 quantile estimate minus the 0.25 quantile estimate) divided by the sum of the 0.75 and 0.25 quantile estimates, the quartile-based coefficient of variation (qCV), which is calculated as the Chla interquartile range divided by the Chla median estimate, or simply as the difference between any selected quantiles. Here, we use qCV as a measure of pixel-wise uncertainty for global mapping and the difference between the 0.75 and 0.25 quantile for visualizing uncertainty at individual locations (see section 5).

In this study, we selected the Box-Cox *t*-distribution (BCTo) as a conditional Chl*a* distribution (Rigby and Stasinopoulos, 2006), because it is a more flexible distribution in terms of representing skewness and kurtosis relative to the lognormal distribution and performed better compared to all alternative distributions examined (Supplementary Table 1). BCTo is a four-parameter distribution with parameters μ,σ,ν,τ, where μ relates to the location (i.e., median), σ to the scale, ν to the skewness and τ to the kurtosis of the distribution (Rigby et al., 2019; Rigby and Stasinopoulos, 2006). This means that μ and σ are defined differently than in the lognormal distribution. A comparison between a BCTo and a lognormal distribution is shown in Fig. 2b. Because the BCTo distribution can model heavier tails than the lognormal distribution, it is more robust to outliers. The BCTo distribution for random variable Y has the probability density function:

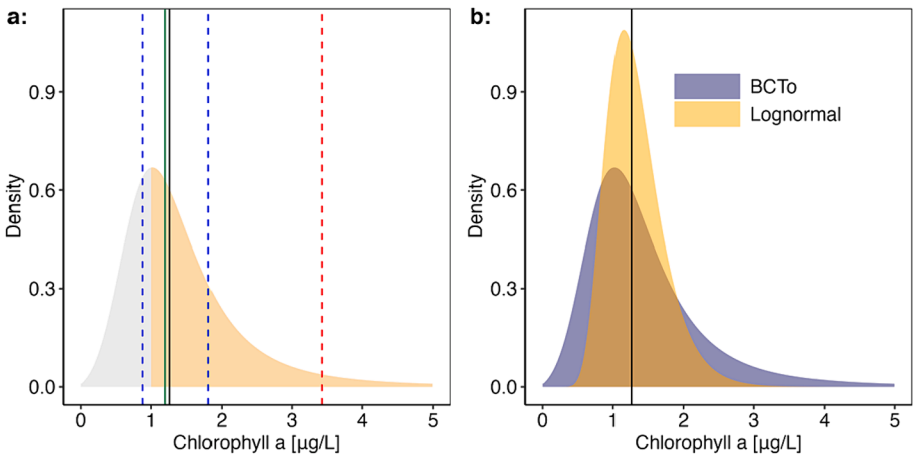

Fig. 2. Principle of GAMLSS estimation and comparison of a BCTo and a lognormal distribution. Panel a) shows how GAMLSS models predict the full conditional distribution (shaded area) of Chl*a* from a single combination of R_{rs} values. This means that in addition to the classical median estimate (black line), GAMLSS can also be used to estimate other quantities, such as the 0.95 quantile (red dashed line) or the 0.25 and 0.75 quantiles (blue dashed lines) useful for quantifying estimation uncertainty. The true chlorophyll-a concentration falls somewhere into this distribution (e.g., green line) The probability of the true Chl*a* value being higher than a chosen threshold e.g., 1 µg/L (orange area) can be calculated from the fitted cumulative distribution function (1 - cdf) at 1 µg/L. Panel b) shows the fitted distribution of a random daily pixel as estimated by the OCG algorithm using a BCTo ($\mu = 1.26$, $\sigma = 0.50$, $\nu = 0.01$, $\tau = 5$) distribution and by the OC3 using a lognormal distribution ($\mu = 1.26$, $\sigma = 0.30$). Note that both algorithms have the same median estimate (black line) in this case. (For interpretation of the references to color in this figure legend, the reader is referred to the web version of this article.)

$$f_Y(y|\mu,\sigma,\nu,\tau) = \frac{y^{\nu-1} f_T(z)}{\mu^{\nu}\sigma F_T\left[(\sigma|\nu|)^{-1}\right]}$$

$$if\,\nu \neq 0, z = \frac{\left(\frac{y}{\mu}\right)^{\nu} - 1}{\sigma\nu} \qquad (1)$$

$$if\,\nu = 0, z = \frac{ln\left(\frac{y}{\mu}\right)}{\sigma}$$

where T has a t-distribution with τ degrees of freedom and $f_T(.)$ and $F_T(.)$ are the probability density function and cumulative distribution function of T, respectively, and where $\mu > 0$, $\sigma > 0$, $-\infty < \nu < +\infty$ and $\tau > 0$. Note that because $y > 0$ the BCTo distribution models a positive response variable.

GAMLSS then uses link functions to relate the parameters to their explanatory variables, which for μ, σ and τ are the natural logarithm, and for ν the identity link. The log link implies that the fitted OCG model parameter is exponentiated to represent estimates on the original parameter scale.

3.3. Band selection and robustness

We used the Bayesian information criterion (BIC) (Schwarz, 1978) for band selection, which identifies the best tradeoff between maximizing the model likelihood and minimizing the number of parameters in the model to find a parsimonious model that avoids overfitting (Konishi and Kitagawa, 2008). BIC is asymptotically equivalent to a leave-many-out cross-validation (Shao, 1997). We tested if transformations of bands including the natural logarithm and power transformations including those to the power of 0.1, 0.2, 0.3, 1/3, 0.4, 0.5, 0.6, 0.7, 2/3, 0.8, 0.9, 1 and −1 improve the model fit. Each band could be included in the model for each distribution parameter μ, σ, ν, τ using any of the transformations described above, but a band could only appear once in the model for each parameter. Because the tested power transformations only build a subset of all possible transformations, we also investigated whether a non-linear P-spline (smoothing spline), that can also capture non-monotonic relationships, was superior to any of the above-tested transformations (Stasinopoulos et al., 2017). The model with the band combination exhibiting the lowest BIC is selected as the final model in a stepwise selection procedure (Stasinopoulos and Rigby, 2007).

We assessed the robustness of band selection by bootstrapping the data used to fit the OCG 1000 times. Bootstrapping resembles cross-validation but does not explicitly divide the data into an *a priori* training and test dataset (James et al., 2013). In each of the 1000 bootstrap samples, observations are selected randomly with replacement until the same number of observations is reached as in the original data. Analogous to cross-validation, bias and accuracy (see section 3.3.1) can thus be evaluated on both the observations used for refitting and band selection (B_{train}) and the observations not included by chance in a particular bootstrapped set (B_{test}) (on average 36.8 % of the observations based on Efron and Tibshirani, 1997). Selected bands for each parameter (i.e., μ, σ, ν, τ) and their transformations in those 1000 bootstrap runs were compared to those in the original model selection to assess the statistical marginal robustness (i.e., significance) of a band in the final model.

3.4. Benchmarking and validation

We compared the OCG algorithm to the original OC3 and OC2 as well as their Color Index corrected versions. Because the current OC algorithms are fitted on different data than the ones used in this study, we also refitted the OC3 and OC2 algorithms on the data used here (see section 2) under the assumptions of a lognormal conditional distribution as well as a Box-Cox t-distribution (BCTo). We also adjusted the four refitted OC algorithms by the Color Index, but this had no significant effect on model performance (not shown).

3.4.1. Comparing the performance of Chla estimates

To compare the different models based on their median Chl*a* estimates, we used the median symmetric accuracy (MdSA) to quantify accuracy and the signed systematic percentage bias (SSPB) to quantify bias (Morley et al., 2018; Pahlevan et al., 2022; Werther et al., 2022a). These are defined as:

$$MdSA = 100(\exp(\mathrm{M}(|\ln \mathrm{Q_i}|)) - 1) \qquad (2)$$

$$SSPB = 100\ \mathrm{sgn}(M(\ln \mathrm{Q_i}))(\exp(|\mathrm{M}(\ln \mathrm{Q_i})|) - 1) \qquad (3)$$

where M(.) represents the median function, sgn(.) the sign function and $Q_i = \hat{m}_i/y_i$, where $\hat{m}$ is the median Chl*a* estimate and y the observed Chl*a* value, i is the data point index, and ln() is the natural log.

The MdSA can be interpreted as the median percent increase from the smaller value of the estimated and observed Chl*a* pair to the larger of these two, while a positive SSPB can be interpreted as the median percent change from the observed to the estimated Chl*a* value. Additionally, we also calculated the commonly used Root Mean Squared Logarithmic Error (RMSLE) to assess accuracy, which represents the Root Mean Squared error on $\log_{10}$ Chl*a* (O'Reilly and Werdell, 2019).

Further, we were interested in how the algorithms compare at different Chl*a* magnitudes. For this, we divided the Chl*a* median estimates into bins in analogy to the Trophic State Index for the freshwater systems (Carlson, 1977; Pahlevan et al., 2020).

We also grouped the data based on their bathymetry, which allowed us to compare the difference in performance in the open ocean versus coastal regions. We selected 130 m as the bathymetry threshold to group the data into coastal and open ocean samples, as this represents the typical depth for continental shelf breaks (Pinet, 2003).

To gauge how the new OCG approach would compare against OC algorithms when retrained on new data available in the future, we also calculated MdSA, SSPB, and RMSLE for the fitted models during bootstrapping on B_{test} (see section 3.2). This bootstrapping approach has several advantages (James et al., 2013) over common held-out approaches (O'Shea et al., 2021; Smith et al., 2021; Werther et al., 2022a). An obvious disadvantage of held-out approaches is that it is a significant waste of data (Steyerberg, 2018), as only a portion of the available data is used to fit the model. Moreover, it is unclear how to optimally split the data (Harrell et al., 1996; Steyerberg et al., 2001). The B_{test} data sets created under bootstrapping instead represent many (e.g., 1000) test data sets, making it possible to quantify the uncertainty in the performance metrics. Moreover, bootstrapping not only tests if specific parameterizations (i.e., coefficients, selected bands) of two algorithms lead to differences in performance, but by refitting the OCG and OC algorithms in each bootstrapping iteration bootstrapping compares the overall performance of the OCG approach to that of the OC approach.

3.4.2. Comparing models based on BIC and distributional assumptions

For the OCG algorithm trained on the original data as well as for the refitted OC algorithms, we compare their BIC values as an additional assessment of model performance. Generally, a BIC difference of two constitutes evidence that one model is better than the other, while a difference greater than ten indicates a very strong difference in the performance (Burnham et al., 2002; Raftery, 1995). This comparison is frequently used as a stand-alone comparison in many research fields such as ecology or medicine (Aho et al., 2014; Brewer et al., 2016; Chowdhury and Turin, 2020).

We also investigated how well the fitted conditional Chl*a* distribution matches the observations, which is needed to accurately estimate uncertainty, quantiles, and Chl*a* exceedance probabilities. For this, we compared the sample quantiles with the theoretical quantiles via detrended Quantile-Quantile plots. Calculations are based on normalized quantile residuals (or z-scores) (Dunn and Smyth, 1996; van Buuren and Fredriks, 2001). A quantile residual is calculated by inserting the observed value of the response variable (Chl*a*) into its cumulative distribution function that is expected for its R_{rs} values, thus representing the quantile that the observed value represents in the fit. The true quantile residual values are uniformly distributed but are transformed to z-scores by inserting the quantile residuals into the inverse cdf of the standard normal distribution. The deviations of the ordered normalized quantile residuals from their expected normal quantiles are then plotted against the expected normal quantiles (Stasinopoulos et al., 2022).

4. Model parameterization and performance

4.1. Model parameterization

The final OCG algorithm as fitted on the 2069 available *in situ* HPLC Chl*a* measurements, with bands selected via BIC, is given by Chl*a* having a Box-Cox *t*-distribution, BCTo(μ, σ, ν, τ):

$$\mu = exp\Big(-19.2 + 28.3\sqrt{R_{rs}(412)} - 240.1R_{rs}(443) - 2.4ln(R_{rs}(488)) \Big) \\ -333.2R_{rs}(547) + 114.5\sqrt{R_{rs}(555)} + 6.8\sqrt{R_{rs}(667)}\Big) \tag{4}$$

$$\sigma = \exp(0.8 - 32.6R_{rs}(443) + 0.2ln(R_{rs}(555))) \tag{5}$$

$$\upsilon = 0.2 - 62.9R_{rs}(412) \tag{6}$$

$$\tau = \exp(1.6) \cong 5.0 \tag{7}$$

where μ represents the median estimate of Chl*a* [μg/L], while σ, υ and τ model the scale and shape (skewness and kurtosis) of the BCTo distribution and are unitless. Note that coefficients are rounded here to the first decimal place and that the code provided with this study should be used for accurate estimates of Chl*a* and uncertainty (see code accessibility). The partial effects that show the relationship of the explanatory variables to the predictors of the response variable distribution parameters (i.e., log μ, log σ, ν, and log τ) are shown in Fig. 3. We assume the covariance structure of bands does not change over space or time such that multicollinearity between bands does not impact future model performance; however, this assumption would need to be retested under future ocean conditions. Due to the inter-band correlations, especially those for the parameter μ, we abstain from drawing any inference on the functional relationships between Chl*a* and the individual bands.

For the parameter μ (Eq. (1) and (4), the transformed bands $\sqrt{R_{rs}(412)}$, $R_{rs}(443)$, ln $R_{rs}(488)$, $R_{rs}(547)$, $\sqrt{R_{rs}(555)}$, and $\sqrt{R_{rs}(667)}$ were selected via BIC. The bands $R_{rs}(443)$, $R_{rs}(488)$, and $R_{rs}(547)$ represent bands that are also part of the classical OC-family of algorithms (O'Reilly et al., 1998; O'Reilly and Werdell, 2019). The green band $R_{rs}(555)$ lies very close to $R_{rs}(547)$, but its square root transform still increases the likelihood of the model without overfitting as indicated during bootstrapping (see section 4.2). The band $R_{rs}(412)$ lies in the violet light spectrum and is often the brightest band detected over the open ocean (O'Reilly and Werdell, 2019). The square root transformation indicates the contribution of the band to the estimate of μ saturates on the log link scale. This also holds for the $R_{rs}(667)$ band, which lies close to the second absorption peak of chlorophyll-*a* (Bricaud et al., 1998). The use of bands close to 412 nm and 670 nm was explored in a recent study and its use in chlorophyll-*a* algorithms encouraged (O'Reilly and Werdell, 2019), further supporting our findings.

For the scale parameter σ (Eq. (1) and (5), $R_{rs}(443)$ and ln $R_{rs}(555)$ are selected in the final model. The scale parameter represents the dispersion parameter for the BCTo distribution; thus, these bands impact the Chl*a* uncertainty (qCV) directly. The untransformed band $R_{rs}(412)$ is selected as the only variable in the model for the skewness parameter ν (Eq. (1) and (6) of the Chl*a* distribution. A decreasing ν increases the skewness and hence the heaviness of the right tail of the BCTo distribution, thus making $R_{rs}(412)$ also an important variable in quantifying the upper percentiles of Chl*a* (extreme events). No band was selected for τ (Eq. (1) and (7), such that τ was constant at 5.0, revealing that the distribution is highly leptokurtic with heavy tails. The fitted median of the OCG model is consistent with the observed Chl*a* (Supplementary Figure 2). The coefficients of the OC2 and OC3 refits are depicted in Supplementary Table 2.

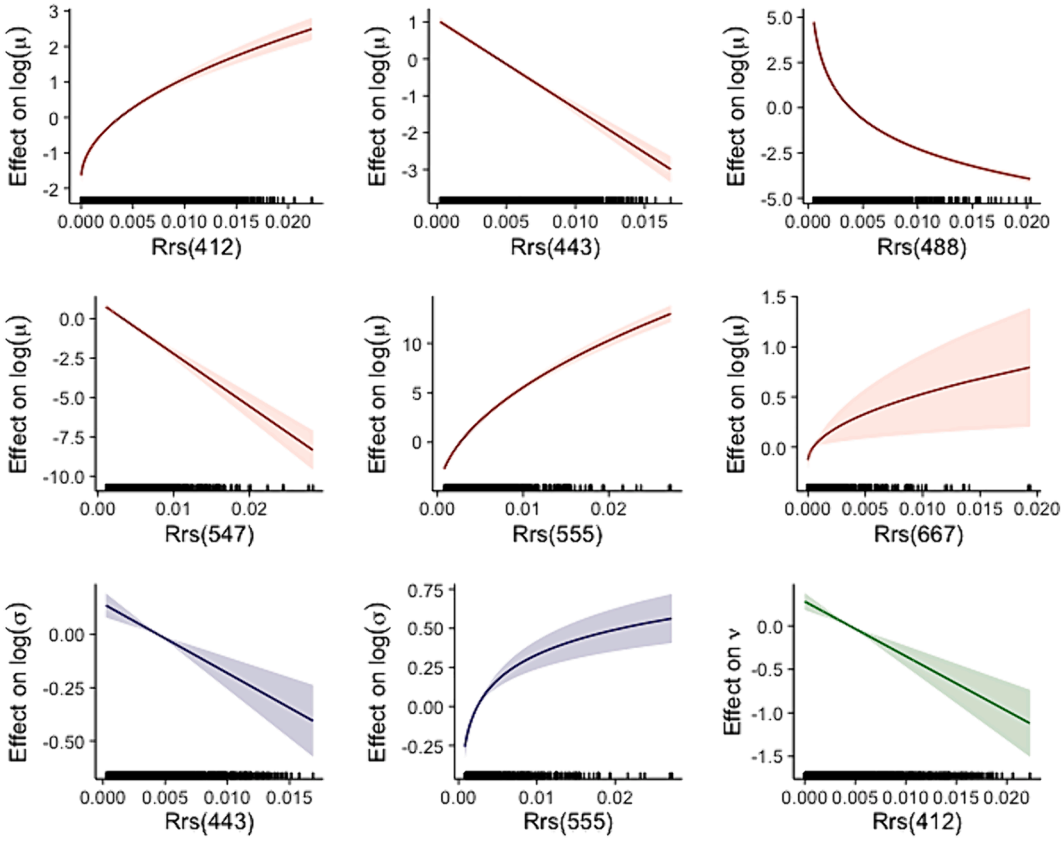

Fig. 3. Partial effects of the bands on the predictors of the parameters, i.e., log μ (red), log σ (blue), and ν (green). The shaded areas correspond to the 95% confidence intervals. The black tick marks along the horizontal axis represent the distribution of data points. Inference from these plots should be done with caution as the bands are correlated, especially $R_{rs}(547)$ and $R_{rs}(555)$. (For interpretation of the references to color in this figure legend, the reader is referred to the web version of this article.)

4.2. Robustness of band selection

Bootstrapping of the band selection process (see section 3.3) indicates that for the parameter μ, the blue and green bands $\sqrt{R_{rs}(412)}$, $R_{rs}(443)$, ln $R_{rs}(488)$, $R_{rs}(547)$, $\sqrt{R_{rs}(555)}$ are all selected very robustly in over 80 % of the 1000 bootstrap samples (Fig. 4). For the red band $\sqrt{R_{rs}(667)}$, this sensitivity analysis shows less consistency. Although $R_{rs}(667)$ is a selected band in over 75 % of bootstrapped samples, its untransformed version is selected almost as often as its square root transformation.

For σ, the bootstrapping analysis reveals that while ln $R_{rs}(555)$ is selected in over 60 % of cases, $R_{rs}(443)$ is not often selected and may be of lesser importance, which needs to be reevaluated when more *in situ* Chl*a* data will be available in the future. The opposite holds for $R_{rs}(547)$, which is not selected in the model of the original data but is selected quite frequently during bootstrapping. For the parameter υ, the violet band $R_{rs}(412)$ is selected in over 60 % of the bootstrap samples, confirming the importance of this band in the algorithm and the estimate of Chl*a* and pixel-wise uncertainty.

Transformations of bands are commonly and robustly selected during bootstrapping; however, especially the log transformation (e.g., $R_{rs}(488)$) for μ may produce outliers when their value approaches zero. This is not a problem unique to the OCG algorithm; it is also observed in classical OC algorithms when the blue-green ratio nears zero and the logarithm becomes undefined. To minimize the impact of this issue, we recommend carefully evaluating Chl*a* estimates at very low R_{rs} magnitudes or only analyzing pixels above a predefined intensity threshold, e.g., $R_{rs}(488) > 0.0001$. Here, no $R_{rs}(488)$ values below this threshold were present, and the use of such a threshold was therefore unnecessary.

4.3. Comparison of the Chla median estimate performance

The final OCG algorithm (Eq. (1), 4, 5, 6, 7) outperforms existing models, including the Color Index corrected OC2 and OC3 and the refitted OC2 and OC3 algorithms under both a lognormal (Fig. 5, green diamonds) and a BCTo distribution (Supplementary Figure 3). Overall, the OCG model leads to an MdSA of 40 %, a RMSLE of 0.27, and a SSPB of below 1 %, while the CI OC3 has an MdSA of 49 %, a RMSLE of 0.32, and a SSPB of over 12 % (Fig. 5, Supplementary Table 3).

Assessing the performance for open ocean versus coastal regions reveals that the high biases (SSPB) in the OC algorithms are originating from coastal regions (Fig. 5a, Supplementary Table 3), where the CI OC3 reaches an SSPB value of 41 %. This bias is inherent to the OC algorithm approach in general, as evident from the SSPB distribution of 1000 bootstrapping runs in the original and refitted OC algorithms (Fig. 5a, violins). In contrast, the OCG algorithm only exhibits a 5 % SSPB, and the bootstrapping analysis shows that both small positive or small negative biases occur across the bootstrapped samples, indicating no consistent bias. For the open ocean, all algorithms have low bias except for Chl*a* estimates above 2.6 μg/L (Fig. 5a, largest orange dots, Supplementary Figure 3) where CI OC2 and CI OC3 exhibit a clear positive SSPB.

In coastal regions, the accuracy of the OCG algorithm as represented by MdSA is more than 20 % better than that of the CI OC3 algorithm (Fig. 5b), while in the open ocean, it is comparable to OC algorithms. The OCG algorithm also consistently exhibits a lower RMSLE than the CI OC3 (Fig. 5c), with a 0.31 RMLSE for coastal regions and a 0.24 RMLSE for the open ocean, compared to the CI OC3 algorithms' 0.37 and 0.28 RMSLE, respectively. We also find that the accuracy is lowest for Chl*a* estimates > 2.6 μg/L across all algorithms for the open ocean (Fig. 5b,c).

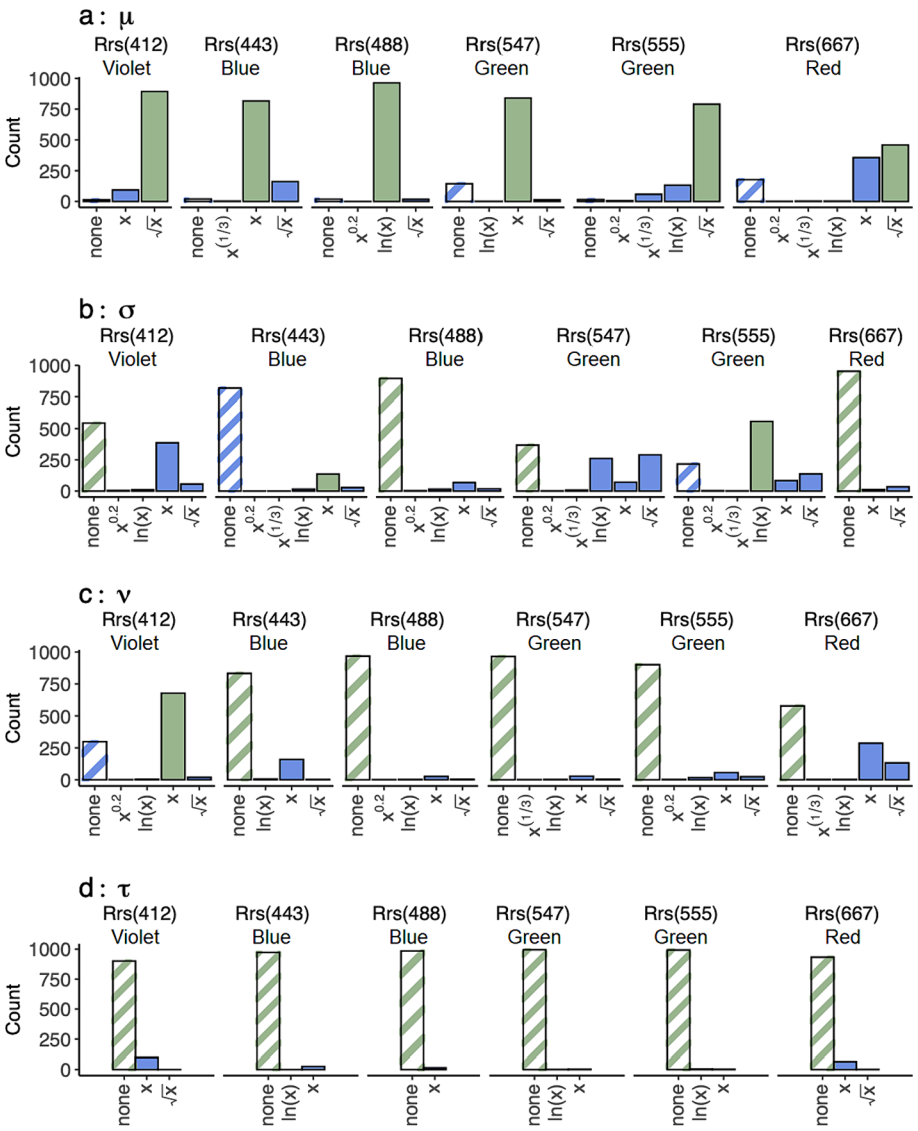

Fig. 4. Sensitivity analysis of the band selection process for the OCG algorithm (Eq. (1). Bars indicate how often a band and its transformation were selected for each parameter during bootstrapping. The band transformation used in the final OCG algorithm based on the non-bootstrapped data is colored green. The diagonal lines indicate cases where a band was not selected. If a power transformation is not listed in a panel, it was not selected at all throughout the bootstrapping. Similarly, P-splines were never selected during bootstrapping. (For interpretation of the references to color in this figure legend, the reader is referred to the web version of this article.)

However, an independent median regression (Fasiolo et al., 2021) of the model residuals plotted against the model log-median estimate, reveals a better fit for the OCG algorithm throughout the full Chl*a* range and in particular under eutrophic conditions (Fig. 6, Supplementary Fig. 4).

The evaluation when using independent non-HPLC data, i.e., observations made using other approaches (see section 2), further supports the OCG algorithm's superior performance (Fig. 5, Supplementary Figure 3, blue squares). It is interesting to note that, independent of the algorithm, fluorometric and spectrophotometric approaches compare generally poorly in coastal regions. However, this is more likely an issue related to the accuracy of these Chl*a* measurements in coastal regions (Pinckney et al., 1994).

4.4. Comparison of BIC and distributional assumptions

Despite having more parameters, the BIC of the OCG fitted on the complete data is significantly lower than the BIC of all the refitted OC models, indicating that the improvement in fit outweighs the increase in model complexity. For example, the refitted OC2 and OC3 algorithms using a BCTo distribution have a BIC that is 424 and 528 above that of the OCG algorithm, respectively. The refitted OC2 and OC3 algorithms using the original lognormal distribution have BICs that are 552 and 691 above those of the OCG algorithm. Given that a difference of 10 represents strong evidence of a superior model (Burnham et al., 2002; Raftery, 1995), the differences here show unequivocal support for the OCG model (see also section 3.4.2).

We find that the OC2 and OC3, as well as their Color Index corrected versions, deviate from their assumption of a conditional lognormal distribution of Chl*a* (Fig. 6; Supplementary Figure 5). This is true for both the original and refitted OC algorithms that assume a lognormal distribution. This is particularly concerning for the upper tail, which is crucial for estimating the potential magnitude of extreme concentrations, i.e., the upper quantiles of Chl*a*, but also affects the accuracy of other quantiles such as the median estimate (Fig. 5).

5. Illustrative applications

We applied the OCG algorithm to daily global R_{rs} between July 2002

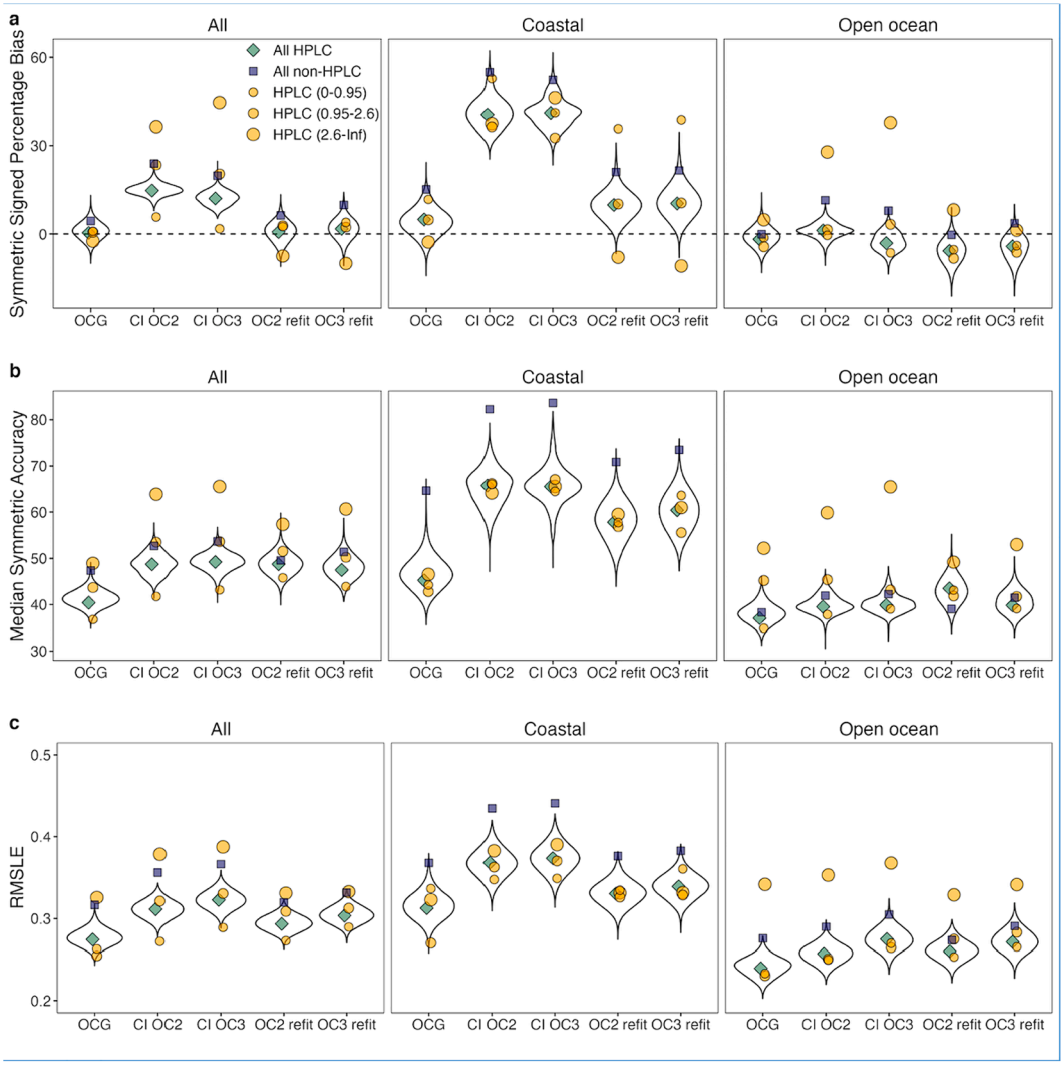

Fig. 5. The OCG algorithm outperforms the OC algorithms in (a) bias (SSPB, Eq. (3), (b) accuracy (MdSA, Eq. (2), and (c) RMSLE. This is especially evident for coastal regions. OC2 and OC3 represent the standard ocean color algorithms, CI OC2 and CI OC3 their Color Index corrected versions. OC2 refit and OC3 refit correspond to the standard ocean color algorithms refitted to the dataset used in this study assuming a lognormal distribution. Green diamonds indicate the SSPB, MdSA, and RMSLE of each algorithm on the complete HPLC data, whereas orange dots show the performance in selected chlorophyll-a bins. The exact values and number of points in each bin are presented in Supplementary Table 3. The blue squares correspond to MdSA, SSPB, and RMSLE estimated on *in situ* chlorophyll-a data that was not based on HPLC measurements and therefore not included in the original model calibration. The violins correspond to the performance metrics calculated on the left-out points during the bootstrapping (B_{test}) and thus represent the distribution of the performance metrics. (For interpretation of the references to color in this figure legend, the reader is referred to the web version of this article.)

and December 2021, and compared estimates to those from the CI OC3 algorithm i.e., the current standard product (Fig. 7a,b).

We find that the OCG algorithm generally estimates higher values of Chl*a* in the open ocean (Fig. 7c); although the absolute magnitude of differences is small for many open ocean regions (e.g., the subtropical gyres), the relative discrepancies are large (Fig. 7d). As subtropical gyres account for approximately 40 % of the Earth surface (McClain et al., 2004), these large relative differences may have huge impacts on our understanding of global carbon cycling (Emerson et al., 1997). Another recent study also reported an underestimation of Chl*a* for the OC algorithms in the tropical Pacific (Pittman et al., 2019). In general, these observed differences are consistent with biases observed based on the Sea-viewing Wide Field-of-view Sensor (SeaWiFS) where the $R_{rs}(412)$ to $R_{rs}(443)$ band ratio was found to be a good indicator for the direction of this bias (Szeto et al., 2011), further emphasizing the benefit of including $R_{rs}(412)$ in the OCG algorithm (O'Reilly and Werdell, 2019).

Inspecting the South Pacific Gyre as a specific example, we find that the OCG algorithm estimates markedly higher Chl*a* between 160°W and 145°W (Fig. 8a) compared to the CI OC3 algorithm. On average, daily estimates between July 2002 to December 2021 from the OCG algorithm are 0.0089 μg/L higher. In addition, the OCG algorithm estimates a smoother decrease of Chl*a* towards the center of the gyre. As the South Pacific Gyre represents the largest ocean desert with very low productivity, which is hypothesized to be expanding under global warming (Polovina et al., 2008), the highest accuracy is essential for monitoring this unique ecosystem under climate change. The Chl*a* values within the gyre are usually higher in austral winter, likely resulting from photoacclimation rather than biomass increase (Behrenfeld et al., 2016); however, for the OCG algorithm, this peak is reached slightly earlier compared to the CI OC3 (Supplementary Figure 6), which warrants further investigation in the future. The OCG algorithm also yields higher Chl*a* around Easter Island at the edge of the gyre (Fig. 8a) which may indicate an island mass effect (enhanced phytoplankton concentration near island-reef ecosystems) in this region (Gove et al., 2016) that is underestimated by the CI OC3.

The OCG algorithm also estimates higher Chl*a* in the high-latitude

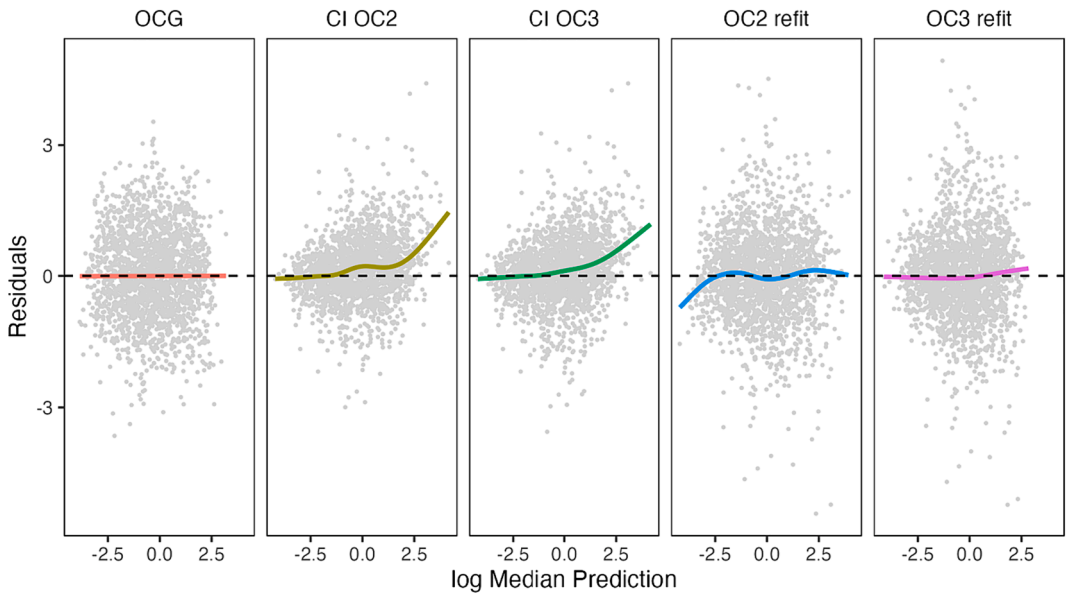

Fig. 6. Independent median regression to model the relationship between normalized quantile residuals of the models and their median estimates shows that the OCG algorithm exhibits no residual outliers or trends. The fit should be as close to a horizontal line as possible centered at zero; otherwise, estimates are biased. CI OC2 and CI OC3 represent the Color Index corrected versions of the standard ocean algorithms. OC2 refit and OC3 refit correspond to the standard ocean color algorithms refitted to the dataset used in this study assuming a lognormal distribution. Gray points indicate quantile residuals.

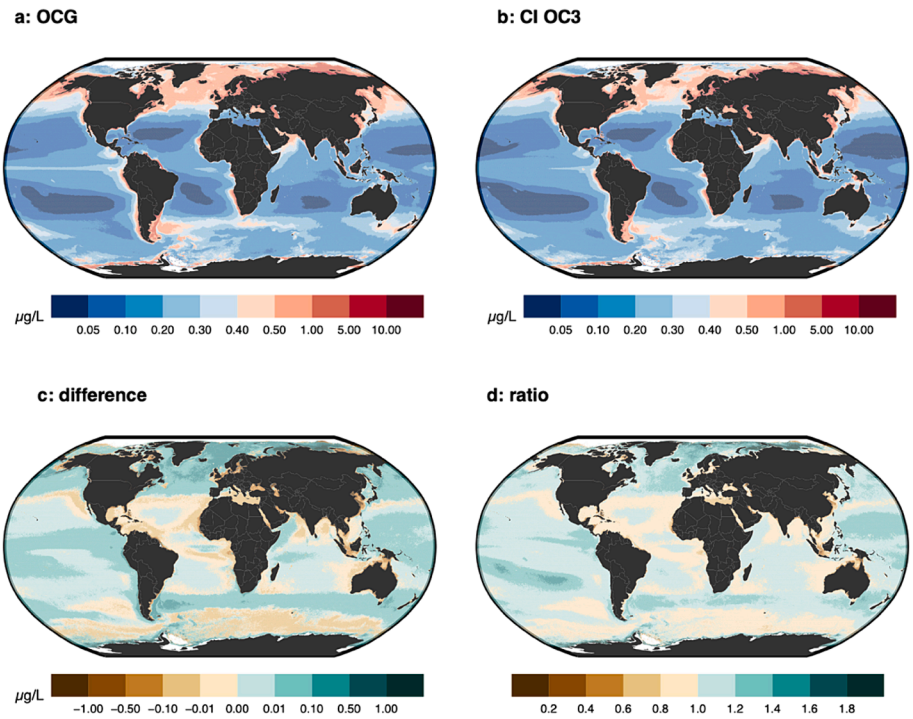

Fig. 7. The OCG algorithm estimates differ from the CI OC3 algorithm in several global regions. Panel a) shows the median across daily OCG estimates at a 4.64 × 4.64 km spatial resolution for July 2002 to December 2021[μg/L]. Panel b) shows the same but for the standard CI OC3 algorithm [μg/L]. Panel c) shows differences [μg/L] between the OCG and CI OC3 algorithms, where green indicates that OCG estimates higher Chl*a* than CI OC3 [μg/L]. Panel d) shows the ratio between a) and b), where green indicates that OCG estimates are higher than those from CI OC3. White areas represent areas with no data. (For interpretation of the references to color in this figure legend, the reader is referred to the web version of this article.)

polar regions, although some Antarctic circumpolar regions show lower estimates relative to the CI OC3 algorithm (Fig. 7). This pattern is consistent with the expected impact of sea ice and special optical water properties on the accuracy of Chl*a* estimates that rely only on the blue-to-green band ratio, such as the OC3 algorithm (Bélanger et al., 2007; Dierssen and Smith, 2000; Zeng et al., 2016), leading to underestimations by these existing algorithms in high Chl*a* regions and overestimations in low Chl*a* regions.

Conversely, the OCG algorithm predicts lower Chl*a* in coastal regions and the oligotrophic Mediterranean Sea (Fig. 7) consistent with the observed positive bias for OC algorithms (Fig. 5a). Previous studies have also shown that OC algorithms overestimate Chl*a* in the Mediterranean

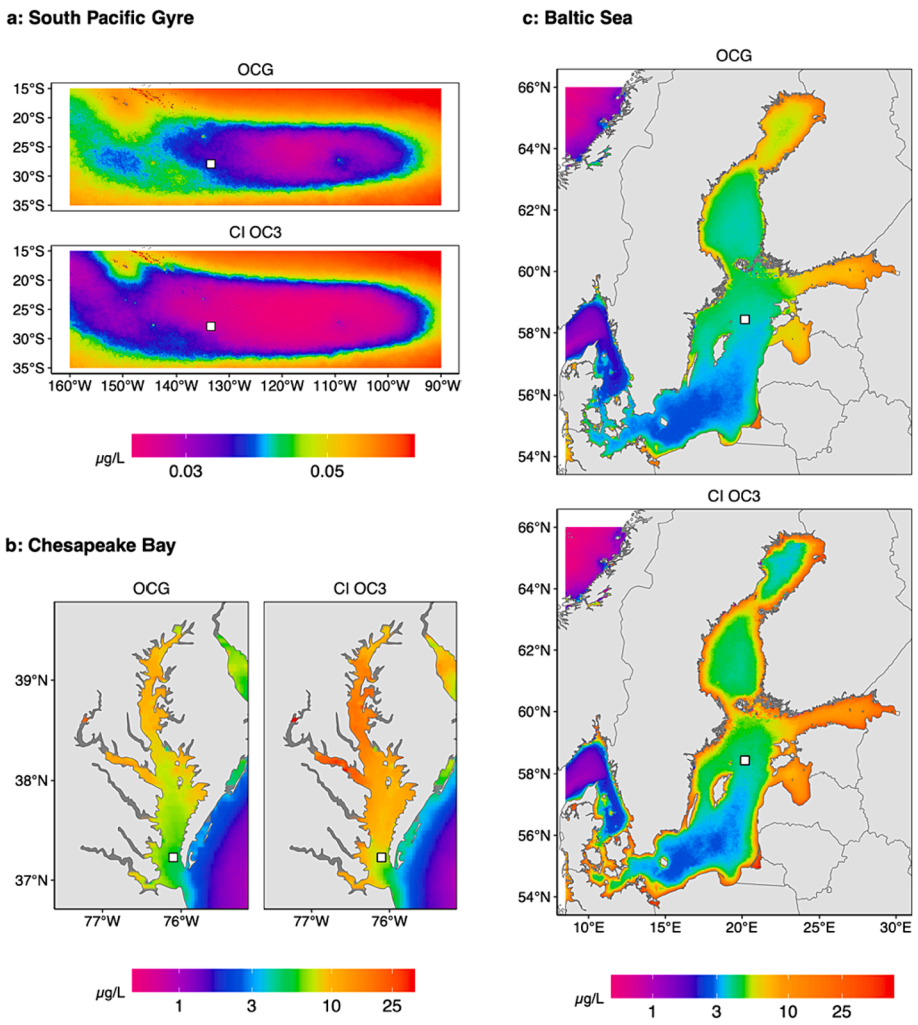

Fig. 8. Selected regional comparisons of the OCG and CI OC3 algorithms. Panels show the median across daily estimates for the period of July 2002 to December 2021 at 4.64 × 4.64 km spatial resolution with estimates for (a) the South Pacific Gyre, (b) the Chesapeake Bay, and (c) the Baltic Sea. The white squares correspond to the pixels chosen for visualizing the time series plots in Fig. 10 and Supplementary Figure 6.

Sea (Volpe et al., 2007), further supporting the performance of the OCG algorithm. Similarly, overestimations in coastal or Case 2 regions with complex optical properties have also been reported previously for OC algorithms (Darecki and Stramski, 2004; McKee et al., 2007; Novoa et al., 2012; Tzortziou et al., 2007; Wynne et al., 2022).

Using the Chesapeake Bay and Baltic Sea as specific examples, the OCG algorithm predicts a smoother transition towards land, indicating that the OCG algorithm is less impacted by low bathymetry and high concentrations of dissolved organic matter (Fig. 8b,c). The OCG algorithm estimates between 2002 and 2021 are on average 2.9 μg/L lower for the Chesapeake Bay and 3.7 μg/L lower across the Baltic Sea relative to the CI OC3 algorithm, matching overestimations observed for CI OC3 (Tzortziou et al., 2007; Werdell et al., 2009). In addition, the OCG algorithm predicts a smoother seasonality in these regions (Supplementary Figure 6).

As described in section 3.2, the OCG algorithm predicts the full conditional distribution of Chl*a*. This enables deeper insights into the discrepancies observed between the two algorithms by calculating which quantile the CI OC3 estimate represents in the conditional distribution of Chl*a* predicted by the OCG algorithm. The closer this value is to 0.5, the more similar the median estimates of both algorithms are. When looking at the typical median over daily quantile estimates at each location, the highest discrepancies are evident along global coastlines and in ocean gyres but can now be interpreted in relation to the Chl*a* uncertainty. For the center of the South Pacific Gyre, for example, the CI OC3 represents an OCG quantile estimate below 0.1 (Fig. 9a,b), indicating that the CI OC3 is predicting very low and unlikely values. In other words, the probability for those locations to have Chl*a* greater than the CI OC3 is typically over 90 % according to the OCG algorithm. Conversely, for parts of Southeast Asia and Oceania, the quantile that CI OC3 estimates represent in the OCG algorithm can be greater than 0.9, indicating that CI OC3 estimates are very high and would be rather rare (occurring less than 10 % of the time) based on the OCG algorithm. On average, the typical estimate from the CI OC3 falls at the 0.42 quantile of the OCG algorithm estimate, although there is considerable geographic variability (Fig. 9b).

The estimate of the full conditional distribution of Chl*a* also makes it possible to quantify per-pixel uncertainty for every estimation time and location. This is illustrated in Fig. 10a for a prototypical location in the Chesapeake Bay (see white square in Fig. 8b) for 2017. For this location, the CI OC3 algorithm estimates are frequently above the daily 0.75 quantile estimates of the OCG algorithm, indicating large differences. The CI OC3 algorithm also predicts much higher extremes and variability. We use the quartile-based coefficient of variation (qCV; see section 3.1) as an illustrative example of how uncertainty can be visualized for the OCG algorithm. Typical qCV values globally (median over

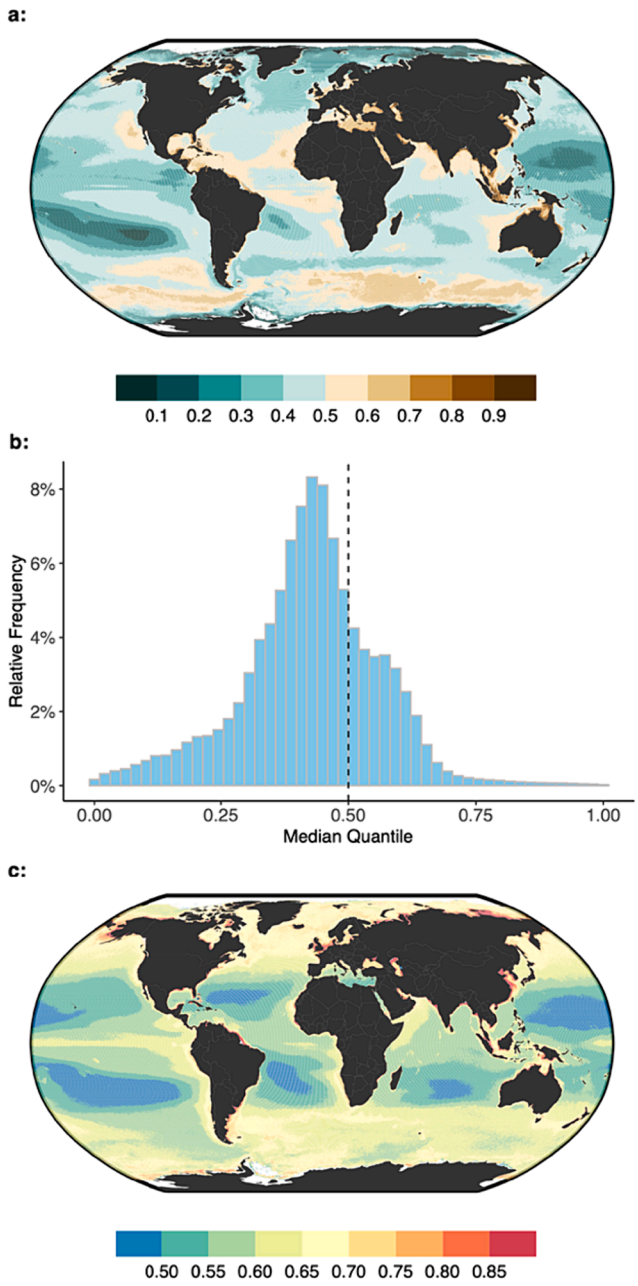

Fig. 9. Fitting the full conditional distribution of chlorophyll-*a* concentrations makes it possible to draw inferences based on the probability distribution of estimated concentrations. Panel (a) shows the median over the period of July 2002 to December 2021 of the quantile of the daily OCG conditional distribution of chlorophyll-a concentrations that corresponds to the CI OC3 estimate for that day. Brown corresponds to regions where the OCG estimates tend to be lower than CI OC3 estimates (mostly coastal regions) while green corresponds to regions where the OCG estimates are higher than CI OC3. Panel (b) shows a histogram of the values presented in panel (a), revealing that for most locations the CI OC3 estimates correspond to OCG quantile estimates below 0.5. This is due to the many open ocean pixels where CI OC3 underestimates Chla. Panel (c) shows the median of the daily qCV [unitless], i.e., the median relative estimation uncertainty of the OCG model, showing that the relative uncertainty of estimates is highest near the coasts. White areas represent areas with no data. (For interpretation of the references to color in this figure legend, the reader is referred to the web version of this article.)

daily qCV estimates for each location) are lowest for the ocean gyres and highest along the coasts (Fig. 9c), which is consistent with the transition from Case 1 to Case 2 waters where Chl*a* becomes higher and the inherent optical water properties are more affected by dissolved organic matter and inorganic contents (IOCCG, 2000). Areas such as the North Sea or the East Sea exhibit the highest qCV (Fig. 9c), which means that in those regions the uncertainty of Chl*a* relative to its median estimate is very large.

The ability to characterize the full conditional distribution of the predicted Chl*a* also opens the door to additional types of analyses as mentioned before. The OCG algorithm can be used to quantify the probability of exceeding any particular Chl*a* threshold. Fig. 10b gives an example of such an application, showing the daily probability of exceedance for three Chl*a* thresholds in 2017 for the same location in the Chesapeake Bay as in Fig. 10a. In this way, the OCG algorithm expands the toolbox for monitoring marine ecosystems and for water quality assessment. Estimating specific quantiles (e.g., the 0.95 quantile) may also be valuable in assessing possible high Chl*a* magnitudes observed in harmful algal blooms.

We note that the GAMLSS approach used to create the OCG algorithm can be extended to any ocean color sensor in principle. In the future, with more *in situ* Chl*a* data available, the GAMLSS approach and band selection may also be extended by incorporating interactions between bands or complementary environmental data to further improve the accuracy of Chl*a* estimates or to build models designed for specific taxa such as cyanobacteria.

6. Conclusions

We introduce a novel global Chl*a* algorithm trained on Level-3 products and *in situ* chlorophyll-a concentrations measured by high-performance liquid chromatography. The OCG surpasses the state-of-the-art CI OC3 algorithm in RMSLE in both coastal regions and the open ocean. Improved accuracy over existing algorithms is particularly pronounced in coastal regions, where the OCG achieves a 20 % improvement in accuracy (MSA) and reduces CI OC3 overestimations of 41 % (SSPB) to below 5 %. Our analysis challenges the assumed lognormal distribution used in OC algorithms, and introduces a novel distributional regression framework, using the BCTo distribution to accurately capture the conditional distribution of Chl*a*. This new framework also provides estimates of pixel-wise uncertainty, quantile estimates beyond the median Chl*a*, and exceedance probabilities for Chl*a* thresholds. The transparent distributional regression framework of OCG holds promise for seamless adaptation to current and future sensors or usage of hyperspectral data (Begliomini et al., 2023), enabling enhanced predictions of water quality and harmful algal blooms.

On a global scale, OCG yields reduced Chl*a* concentrations in coastal regions, the Southern Ocean, and the Mediterranean Sea. Conversely, it indicates elevated values in expansive open ocean regions and specifically in ocean gyres and polar regions. Notably, regions like the East Sea and North Sea exhibit the highest relative pixel-wise uncertainties. The features of the OCG offer valuable new opportunities for identifying and reassessing Chl*a* trends during the MODIS Aqua mission and will help advance our understanding of marine ecosystems and ocean productivity.

Code and data accessibility

To provide easy access to the OCG algorithm we supply code in the "R" language to allow easy calculations given Level-3 MODIS Aqua remote sensing reflectance data under https://github.com/JulianMerder/OCG-prediction. We also provide code to show how to fit a GAMLSS model based on the data used in this study (based on Valente et al., 2019).

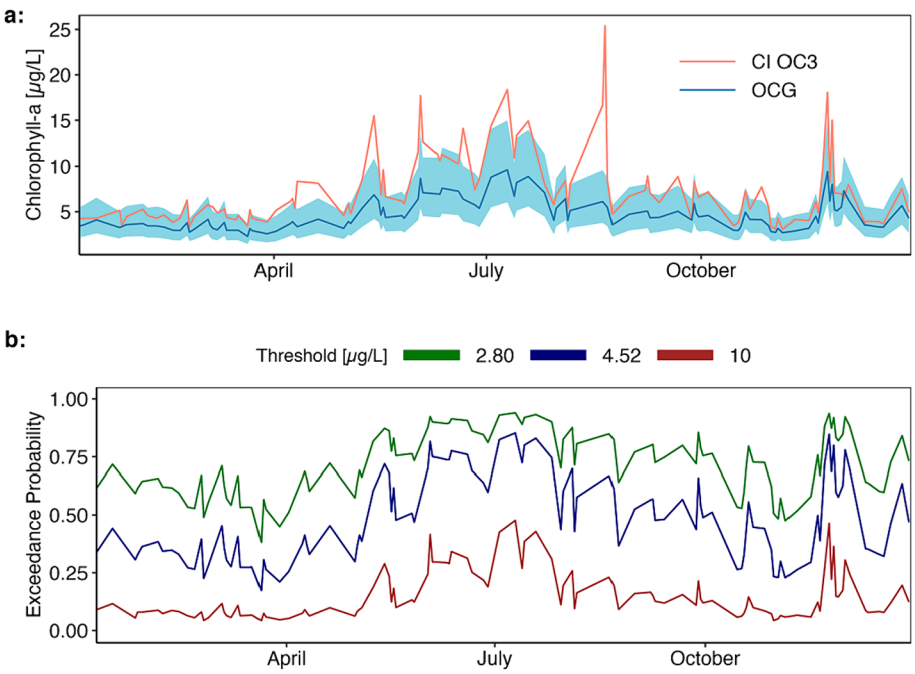

Fig. 10. Examples of daily model estimates for one location in Chesapeake Bay in 2017. Panel (a) illustrates the median estimates for both the OCG and CI OC3 at the location (white square in Fig. 8b). The blue shaded area shows the 0.25 and 0.75 quantile estimates of the OCG algorithm, illustrating the ability to derive location- and day-specific uncertainty bounds on estimates. Panel (b) represents the daily probability of Chla exceeding three specific water quality thresholds based on Maciel et al., (2022) and Williams et al., (2009). (For interpretation of the references to color in this figure legend, the reader is referred to the web version of this article.)

Declaration of competing interest

The authors declare that they have no known competing financial interests or personal relationships that could have appeared to influence the work reported in this paper.

Acknowledgments

We thank the NASA Goddard Space Flight Center, particularly the Ocean Biology Processing Group, for making remote sensing data accessible. Nima Pahlevan was funded under the NASA ROSES grant #80NSSC22K1389, Remote Sensing of water quality 2021.

Appendix A. Supplementary data

Supplementary data to this article can be found online at https://doi.org/10.1016/j.isprsjprs.2024.03.014.

References

Aho, K., Derryberry, D., Peterson, T., 2014. Model selection for ecologists: the worldviews of AIC and BIC. Ecology 95, 631–636. https://doi.org/10.1890/13-1452.1.

Al Shehhi, M.R., Gherboudj, I., Zhao, J., Ghedira, H., 2017. Improved atmospheric correction and chlorophyll-a remote sensing models for turbid waters in a dusty environment. ISPRS J. Photogramm. Remote Sens. 133, 46–60. https://doi.org/10.1016/j.isprsjprs.2017.09.011.

Bauer, J.E., Cai, W.-J., Raymond, P.A., Bianchi, T.S., Hopkinson, C.S., Regnier, P.A.G., 2013. The changing carbon cycle of the coastal ocean. Nature 504, 61–70. https://doi.org/10.1038/nature12857.

Begliomini, F.N., Barbosa, C.C.F., Martins, V.S., Novo, E.M.L.M., Paulino, R.S., Maciel, D. A., Lima, T.M.A., O'Shea, R.E., Pahlevan, N., Lamparelli, M.C., 2023. Machine learning for cyanobacteria mapping on tropical urban reservoirs using PRISMA hyperspectral data. ISPRS J. Photogramm. Remote Sens. 204, 378–396. https://doi.org/10.1016/j.isprsjprs.2023.09.019.

Behrenfeld, M.J., O'Malley, R.T., Boss, E.S., Westberry, T.K., Graff, J.R., Halsey, K.H., Milligan, A.J., Siegel, D.A., Brown, M.B., 2016. Revaluating ocean warming impacts on global phytoplankton. Nat. Clim. Change 6, 323–330. https://doi.org/10.1038/nclimate2838.

Bélanger, S., Ehn, J.K., Babin, M., 2007. Impact of sea ice on the retrieval of water-leaving reflectance, chlorophyll a concentration and inherent optical properties from satellite ocean color data. Remote Sens. Environ. 111, 51–68. https://doi.org/10.1016/j.rse.2007.03.013.

Björn, L.O., Papageorgiou, G.C., Blankenship, R.E., Govindjee, 2009. A viewpoint: why chlorophyll a? Photosynth. Res. 99, 85–98. https://doi.org/10.1007/s11120-008-9395-x.

Bojinski, S., Verstraete, M., Peterson, T.C., Richter, C., Simmons, A., Zemp, M., 2014. The concept of essential climate Variables in support of climate Research, applications, and policy. Bull. Am. Meteorol. Soc. 95, 1431–1443. https://doi.org/10.1175/BAMS-D-13-00047.1.

Brewer, M.J., Butler, A., Cooksley, S.L., 2016. The relative performance of AIC, AIC $_C$ and BIC in the presence of unobserved heterogeneity. Methods Ecol Evol 7, 679–692. https://doi.org/10.1111/2041-210X.12541.

Brewin, R.J.W., Mélin, F., Sathyendranath, S., Steinmetz, F., Chuprin, A., Grant, M., 2014. On the temporal consistency of chlorophyll products derived from three ocean-colour sensors. ISPRS J. Photogramm. Remote Sens. 97, 171–184. https://doi.org/10.1016/j.isprsjprs.2014.08.013.

Brewin, R.J.W., Raitsos, D.E., DallOlmo, G., Zarokanellos, N., Jackson, T., Racault, M.-F., Boss, E.S., Sathyendranath, S., Jones, B.H., Hoteit, I., 2015a. Regional ocean-colour chlorophyll algorithms for the Red Sea. Remote Sens. Environ. 165, 64–85. https://doi.org/10.1016/j.rse.2015.04.024.

Brewin, R.J.W., Sathyendranath, S., Müller, D., Brockmann, C., Deschamps, P.-Y., Devred, E., Doerffer, R., Fomferra, N., Franz, B., Grant, M., Groom, S., Horseman, A., Hu, C., Krasemann, H., Lee, Z., Maritorena, S., Mélin, F., Peters, M., Platt, T., Regner, P., Smyth, T., Steinmetz, F., Swinton, J., Werdell, J., White, G.N., 2015b. The ocean colour climate change initiative: III. a round-robin comparison on in-water bio-optical algorithms. Remote Sens. Environ. 162, 271–294. https://doi.org/10.1016/j.rse.2013.09.016.

Brewin, R.J.W., Sathyendranath, S., Platt, T., Bouman, H., Ciavatta, S., DallOlmo, G., Dingle, J., Groom, S., Jönsson, B., Kostadinov, T.S., Kulk, G., Laine, M., Martínez-Vicente, V., Psarra, S., Raitsos, D.E., Richardson, K., Rio, M.-H., Rousseaux, C.S., Salisbury, J., Shutler, J.D., Walker, P., 2021. Sensing the ocean biological carbon pump from space: a review of capabilities, concepts, research gaps and future developments. Earth Sci. Rev. 217, 103604 https://doi.org/10.1016/j.earscirev.2021.103604.

Bricaud, A., Morel, A., Babin, M., Allali, K., Claustre, H., 1998. Variations of light absorption by suspended particles with chlorophyll a concentration in oceanic (case 1) waters: analysis and implications for bio-optical models. J. Geophys. Res. Oceans 103, 31033–31044.

Burnham, K.P., Anderson, D.R., Burnham, K.P., 2002. Model selection and multimodel inference: a practical information-theoretic approach, 2nd ed. Springer, New York.

Campbell, J.W., 1995. The lognormal distribution as a model for bio-optical variability in the sea. J. Geophys. Res. 100, 13237. https://doi.org/10.1029/95JC00458.

Carlson, R.E., 1977. A trophic state index for lakes1: trophic state index. Limnol. Oceanogr. 22, 361–369. https://doi.org/10.4319/lo.1977.22.2.0361.

Chowdhury, M.Z.I., Turin, T.C., 2020. Variable selection strategies and its importance in clinical prediction modelling. Fam Med Com Health 8, e000262.

Cui, T., Zhang, J., Tang, J., Sathyendranath, S., Groom, S., Ma, Y., Zhao, W., Song, Q., 2014. Assessment of satellite ocean color products of MERIS, MODIS and SeaWiFS along the East China coast (in the Yellow Sea and East China Sea). ISPRS J. Photogramm. Remote Sens. 87, 137–151. https://doi.org/10.1016/j.isprsjprs.2013.10.013.

Darecki, M., Stramski, D., 2004. An evaluation of MODIS and SeaWiFS bio-optical algorithms in the Baltic Sea. Remote Sens. Environ. 89, 326–350. https://doi.org/10.1016/j.rse.2003.10.012.

Dierssen, H.M., Smith, R.C., 2000. Bio-optical properties and remote sensing ocean color algorithms for Antarctic peninsula waters. J. Geophys. Res. 105, 26301–26312. https://doi.org/10.1029/1999JC000296.

Dierssen, H.M., 2010. Perspectives on empirical approaches for ocean color remote sensing of chlorophyll in a changing climate. Proceedings of the National Academy of Sciences 107, 17073–17078. https://doi.org/10.1073/pnas.0913800107.

Dunn, P.K., Smyth, G.K., 1996. Randomized quantile residuals. J. Comput. Graph. Stat. 5, 236. https://doi.org/10.2307/1390802.

Efron, B., Tibshirani, R., 1997. Improvements on cross-validation: the. 632+ bootstrap method. J. Am. Stat. Assoc. 92, 548. https://doi.org/10.2307/2965703.

Emerson, S., Quay, P., Karl, D., Winn, C., Tupas, L., Landry, M., 1997. Experimental determination of the organic carbon flux from open-ocean surface waters. Nature 389, 951–954. https://doi.org/10.1038/40111.

Esaias, W.E., Abbott, M.R., Barton, I., Brown, O.B., Campbell, J.W., Carder, K.L., Clark, D.K., Evans, R.H., Hoge, F.E., Gordon, H.R., Balch, W.M., Letelier, R., Minnett, P.J., 1998. An overview of MODIS capabilities for ocean science observations. IEEE Trans. Geosci. Remote Sensing 36, 1250–1265. https://doi.org/10.1109/36.701076.

Falkowski, P.G., Barber, R.T., Smetacek, V., 1998. Biogeochemical controls and feedbacks on ocean Primary production. Science 281, 200–206. https://doi.org/10.1126/science.281.5374.200.

Fasiolo, M., Wood, S.N., Zaffran, M., Nedellec, R., Goude, Y., 2021. Fast calibrated additive quantile regression. J. Am. Stat. Assoc. 116, 1402–1412. https://doi.org/10.1080/01621459.2020.1725521.

Field, C.B., Behrenfeld, M.J., Randerson, J.T., Falkowski, P., 1998. Primary production of the biosphere: integrating terrestrial and oceanic components. Science 281, 237–240. https://doi.org/10.1126/science.281.5374.237.

Gitelson, A.A., DallOlmo, G., Moses, W., Rundquist, D.C., Barrow, T., Fisher, T.R., Gurlin, D., Holz, J., 2008. A simple semi-analytical model for remote estimation of chlorophyll-a in turbid waters: validation. Remote Sens. Environ. 112, 3582–3593. https://doi.org/10.1016/j.rse.2008.04.015.

Gohin, F., Druon, J.N., Lampert, L., 2002. A five channel chlorophyll concentration algorithm applied to SeaWiFS data processed by SeaDAS in coastal waters. Int. J. Remote Sens. 23, 1639–1661. https://doi.org/10.1080/01431160110071879.

Gokul, E.A., Raitsos, D.E., Gittings, J.A., Alkawri, A., Hoteit, I., 2019. Remotely sensing harmful algal blooms in the Red Sea. PLoS One 14, e0215463.

Gove, J.M., McManus, M.A., Neuheimer, A.B., Polovina, J.J., Drazen, J.C., Smith, C.R., Merrifield, M.A., Friedlander, A.M., Ehses, J.S., Young, C.W., Dillon, A.K., Williams, G.J., 2016. Near-island biological hotspots in barren ocean basins. Nat Commun 7, 10581. https://doi.org/10.1038/ncomms10581.

Groom, S., Sathyendranath, S., Ban, Y., Bernard, S., Brewin, R., Brotas, V., Brockmann, C., Chauhan, P., Choi, J., Chuprin, A., Ciavatta, S., Cipollini, P., Donlon, C., Franz, B., He, X., Hirata, T., Jackson, T., Kampel, M., Krasemann, H., Lavender, S., Pardo-Martinez, S., Mélin, F., Platt, T., Santoleri, R., Skakala, J., Schaeffer, B., Smith, M., Steinmetz, F., Valente, A., Wang, M., 2019. Satellite Ocean Colour: Current Status and Future Perspective. Front. Mar. Sci. 6, 485. https://doi.org/10.3389/fmars.2019.00485.

Hammond, M.L., Beaulieu, C., Henson, S.A., Sahu, S.K., 2018. Assessing the presence of discontinuities in the ocean color satellite record and their effects on chlorophyll trends and their uncertainties. Geophys. Res. Lett. 45, 7654–7662. https://doi.org/10.1029/2017GL076928.

Han, W., Zhang, X., Wang, Y.i., Wang, L., Huang, X., Li, J., Wang, S., Chen, W., Li, X., Feng, R., Fan, R., Zhang, X., Wang, Y., 2023. A survey of machine learning and deep learning in remote sensing of geological environment: challenges, advances, and opportunities. ISPRS J. Photogramm. Remote Sens. 202, 87–113. https://doi.org/10.1016/j.isprsjprs.2023.05.032.

Harrell, F.E., Lee, K.L., Mark, D.B., 1996. Multivariable prognostic models: issues in developing models, evaluating assumptions and adequacy, and measuring and reducing errors. Statist. Med. 15, 361–387. https://doi.org/10.1002/(SICI)1097-0258(19960229)15:4<361::AID-SIM168>3.0.CO;2-4.

Henson, S.A., Sarmiento, J.L., Dunne, J.P., Bopp, L., Lima, I., Doney, S.C., John, J., Beaulieu, C., 2010. Detection of anthropogenic climate change in satellite records of ocean chlorophyll and productivity. Biogeosciences 7, 621–640. https://doi.org/10.5194/bg-7-621-2010.

Hieronymi, M., Müller, D., Doerffer, R., 2017. The OLCI neural network Swarm (ONNS): a bio-geo-optical algorithm for Open Ocean and coastal waters. Front. Mar. Sci. 4, 140. https://doi.org/10.3389/fmars.2017.00140.

Hollmann, R., Merchant, C.J., Saunders, R., Downy, C., Buchwitz, M., Cazenave, A., Chuvieco, E., Defourny, P., de Leeuw, G., Forsberg, R., Holzer-Popp, T., Paul, F., Sandven, S., Sathyendranath, S., van Roozendael, M., Wagner, W., 2013. The ESA climate change initiative: satellite data Records for Essential Climate Variables. Bull. Am. Meteorol. Soc. 94, 1541–1552. https://doi.org/10.1175/BAMS-D-11-00254.1.

Hu, C., Lee, Z., Franz, B., 2012. Chlorophyll a algorithms for oligotrophic oceans: a novel approach based on three-band reflectance difference. J. Geophys. Res. 117 https://doi.org/10.1029/2011JC007395.

Hu, C., Feng, L., Lee, Z., 2013. Uncertainties of SeaWiFS and MODIS remote sensing reflectance: implications from clear water measurements. Remote Sens. Environ. 133, 168–182. https://doi.org/10.1016/j.rse.2013.02.012.

Hu, C., Feng, L., Lee, Z., Franz, B.A., Bailey, S.W., Werdell, P.J., Proctor, C.W., 2019. Improving satellite global chlorophyll *a* data products through algorithm refinement and data recovery. JGR Oceans 124, 1524–1543. https://doi.org/10.1029/2019JC014941.

Huot, Y., Babin, M., Bruyant, F., Grob, C., Twardowski, M.S., Claustre, H., 2007. Relationship between photosynthetic parameters and different proxies of phytoplankton biomass in the subtropical ocean. Biogeosciences 4, 853–868. https://doi.org/10.5194/bg-4-853-2007.

Ioannou, I., Gilerson, A., Gross, B., Moshary, F., Ahmed, S., 2013. Deriving ocean color products using neural networks. Remote Sens. Environ. 134, 78–91. https://doi.org/10.1016/j.rse.2013.02.015.

IOCCG, 2000. Remote Sensing of Ocean Colour in Coastal, and Other Optically-Complex, Waters, (ed. S. Sathyendranath). International Ocean-Colour Coordinating Group (IOCCG), Reports of the International Ocean-Colour Coordinating Group, No. 3, Dartmouth, NS, Canada. https://doi.org/10.25607/OBP-95.

IOCCG, 2006. Remote Sensing of Inherent Optical Properties: Fundamentals, Tests of Algorithms, and Applications, (ed. Z-P. Lee). International Ocean-Colour Coordinating Group (IOCCG), Reports of the International Ocean-Colour Coordinating Group, No. 5, Dartmouth, NS, Canada. https://doi.org/10.25607/OBP-96.

IOCCG, 2007. Ocean-Colour Data Merging. (ed. Gregg, W.). International Ocean-Colour Coordinating Group (IOCCG), Reports of the International Ocean-Colour Coordinating Group, No. 6, Dartmouth, NS, Canada. https://doi.org/10.25607/OBP-100.

IOCCG, 2019. Uncertainties in Ocean Colour Remote Sensing. (ed. Mélin F.) International Ocean-Colour Coordinating Group (IOCCG), Reports of the International Ocean-Colour Coordinating Group, No. 18, Dartmouth, NS, Canada. https://doi.org/10.25607/OBP-696.

James, G., Witten, D., Hastie, T., Tibshirani, R. (Eds.), 2013. An Introduction to Statistical Learning: with Applications in r, Springer Texts in Statistics. Springer, New York.

Konishi, S., Kitagawa, G., 2008. Information criteria and statistical modeling. Springer series in statistics, Springer, New York.

Kress, N., Rahav, E., Silverman, J., Herut, B., 2019. Environmental status of Israel's Mediterranean coastal waters: setting reference conditions and thresholds for nutrients, chlorophyll-a and suspended particulate matter. Mar. Pollut. Bull. 141, 612–620. https://doi.org/10.1016/j.marpolbul.2019.02.070.

Liu, X., Steele, C., Simis, S., Warren, M., Tyler, A., Spyrakos, E., Selmes, N., Hunter, P., 2021. Retrieval of chlorophyll-a concentration and associated product uncertainty in optically diverse lakes and reservoirs. Remote Sens. Environ. 267, 112710 https://doi.org/10.1016/j.rse.2021.112710.

Maciel, F.P., Haakonsson, S., Ponce de León, L., Bonilla, S., Pedocchi, F., 2022. Challenges for chlorophyll-a remote sensing in a highly variable turbidity estuary, an implementation with Sentinel-2. Geocarto Int. 1–26 https://doi.org/10.1080/10106049.2022.2160017.

McClain, C.R., Signorini, S.R., Christian, J.R., 2004. Subtropical gyre variability observed by ocean-color satellites. Deep Sea Res. Part II 51, 281–301. https://doi.org/10.1016/j.dsr2.2003.08.002.

McKee, D., Cunningham, A., Dudek, A., 2007. Optical water type discrimination and tuning remote sensing band-ratio algorithms: application to retrieval of chlorophyll and Kd(490) in the irish and celtic seas. Estuar. Coast. Shelf Sci. 73, 827–834. https://doi.org/10.1016/j.ecss.2007.03.028.

Melin, F., 2010. Global distribution of the random uncertainty associated with satellite-derived chl *a*. IEEE Geosci. Remote Sensing Lett. 7, 220–224. https://doi.org/10.1109/LGRS.2009.2031825.

Mélin, F., Sclep, G., Jackson, T., Sathyendranath, S., 2016. Uncertainty estimates of remote sensing reflectance derived from comparison of ocean color satellite data sets. Remote Sens. Environ. 177, 107–124. https://doi.org/10.1016/j.rse.2016.02.014.

Moore, T.S., Campbell, J.W., Dowell, M.D., 2009. A class-based approach to characterizing and mapping the uncertainty of the MODIS ocean chlorophyll product. Remote Sens. Environ. 113, 2424–2430. https://doi.org/10.1016/j.rse.2009.07.016.

Moradi, M., 2021. Evaluation of merged multi-sensor ocean-color chlorophyll products in the northern persian gulf. Cont. Shelf Res. 221, 104415 https://doi.org/10.1016/j.csr.2021.104415.

Morley, S.K., Brito, T.V., Welling, D.T., 2018. Measures of model performance based on the log Accuracy ratio. Space Weather 16, 69–88. https://doi.org/10.1002/2017SW001669.

NASA Goddard Space Flight Center, Ocean Ecology Laboratory, Ocean Biology Processing Group, 2018. Moderate-resolution Imaging Spectroradiometer (MODIS) Aqua Remote-Sensing Reflectance Data 2018 Reprocessing. https://doi.org/10.5067/AQUA/MODIS/L3M/RRS/2018.

Novoa, S., Chust, G., Sagarminaga, Y., Revilla, M., Borja, A., Franco, J., 2012. Water quality assessment using satellite-derived chlorophyll-a within the european directives, in the southeastern Bay of Biscay. Mar. Pollut. Bull. 64, 739–750. https://doi.org/10.1016/j.marpolbul.2012.01.020.

O'Reilly, J.E., Maritorena, S., Mitchell, B.G., Siegel, D.A., Carder, K.L., Garver, S.A., Kahru, M., McClain, C., 1998. Ocean color chlorophyll algorithms for SeaWiFS. J. Geophys. Res. 103, 24937–24953. https://doi.org/10.1029/98JC02160.

O'Reilly, J.E., Werdell, P.J., 2019. Chlorophyll algorithms for ocean color sensors - OC4, OC5 & OC6. Remote Sens. Environ. 229, 32–47. https://doi.org/10.1016/j.rse.2019.04.021.

O'Shea, R.E., Pahlevan, N., Smith, B., Bresciani, M., Egerton, T., Giardino, C., Li, L., Moore, T., Ruiz-Verdu, A., Ruberg, S., Simis, S.G.H., Stumpf, R., Vaičiūtė, D., 2021. Advancing cyanobacteria biomass estimation from hyperspectral observations:

demonstrations with HICO and PRISMA imagery. Remote Sens. Environ. 266, 112693 https://doi.org/10.1016/j.rse.2021.112693.
Pahlevan, N., Smith, B., Schalles, J., Binding, C., Cao, Z., Ma, R., Alikas, K., Kangro, K., Gurlin, D., Hà, N., Matsushita, B., Moses, W., Greb, S., Lehmann, M.K., Ondrusek, M., Oppelt, N., Stumpf, R., 2020. Seamless retrievals of chlorophyll-a from Sentinel-2 (MSI) and Sentinel-3 (OLCI) in inland and coastal waters: a machine-learning approach. Remote Sens. Environ. 240, 111604 https://doi.org/10.1016/j.rse.2019.111604.
Pahlevan, N., Smith, B., Alikas, K., Anstee, J., Barbosa, C., Binding, C., Bresciani, M., Cremella, B., Giardino, C., Gurlin, D., Fernandez, V., Jamet, C., Kangro, K., Lehmann, M.K., Loisel, H., Matsushita, B., Hà, N., Olmanson, L., Potvin, G., Simis, S. G.H., VanderWoude, A., Vantrepotte, V., Ruiz-Verdù, A., 2022. Simultaneous retrieval of selected optical water quality indicators from Landsat-8, Sentinel-2, and Sentinel-3. Remote Sens. Environ. 270, 112860 https://doi.org/10.1016/j.rse.2021.112860.
Pauly, D., Christensen, V., Guénette, S., Pitcher, T.J., Sumaila, U.R., Walters, C.J., Watson, R., Zeller, D., 2002. Towards sustainability in world fisheries. Nature 418, 689–695. https://doi.org/10.1038/nature01017.
Pinckney, J., Papa, R., Zingmark, R., 1994. Comparison of high-performance liquid chromatographic, spectrophotometric, and fluorometric methods for determining chlorophyll a concentrations in estaurine sediments. J. Microbiol. Methods 19, 59–66. https://doi.org/10.1016/0167-7012(94)90026-4.
Pinet, P.R., 2003. Invitation to oceanography, 3rd ed. Jones and Bartlett Publishers, Boston.
Pittman, N.A., Strutton, P.G., Johnson, R., Matear, R.J., 2019. An assessment and improvement of Satellite Ocean color algorithms for the tropical Pacific Ocean. J. Geophys. Res. Oceans 124, 9020–9039. https://doi.org/10.1029/2019JC015498.
Polovina, J.J., Howell, E.A., Abecassis, M., 2008. Ocean's least productive waters are expanding. Geophys. Res. Lett. 35, L03618. https://doi.org/10.1029/2007GL031745.
Raftery, A.E., 1995. Bayesian model selection in social Research. Sociol. Methodol. 25, 111. https://doi.org/10.2307/271063.
Rigby, R.A., Stasinopoulos, D.M., 2005. Generalized additive models for location, scale and shape (with discussion). J Royal Statistical Soc C 54, 507–554. https://doi.org/10.1111/j.1467-9876.2005.00510.x.
Rigby, R.A., Stasinopoulos, D.M., 2006. Using the box-cox t distribution in GAMLSS to model skewness and kurtosis. Stat. Model. 6, 209–229. https://doi.org/10.1191/1471082X06st122oa.
Rigby, R.A., Stasinopoulos, M.D., Heller, G.Z., De Bastiani, F., 2019. Distribution for modelling location, scale, and shape: using GAMLSS in R, Chapman & Hall/CRC : the R series. CRC Press, Bocat Raton, Florida.
Rudin, C., 2019. Stop explaining black box machine learning models for high stakes decisions and use interpretable models instead. Nat Mach Intell 1, 206–215. https://doi.org/10.1038/s42256-019-0048-x.
Saranathan, A.M., Smith, B., Pahlevan, N., 2023. Per-pixel uncertainty quantification and reporting for satellite-derived chlorophyll-a estimates via mixture density networks. IEEE Trans. Geosci. Remote Sensing 1–1. https://doi.org/10.1109/TGRS.2023.3234465.
Savtchenko, A., Ouzounov, D., Ahmad, S., Acker, J., Leptoukh, G., Koziana, J., Nickless, D., 2004. Terra and Aqua MODIS products available from NASA GES DAAC. Adv. Space Res. 34, 710–714. https://doi.org/10.1016/j.asr.2004.03.012.
Schwarz, G., 1978. Estimating the dimension of a model. The Annals of Statistics 6. https://doi.org/10.1214/aos/1176344136.
Scott, J.P., Werdell, P.J., 2019. Comparing level-2 and level-3 satellite ocean color retrieval validation methodologies. Opt. Express 27, 30140. https://doi.org/10.1364/OE.27.030140.
Seegers, B.N., Stumpf, R.P., Schaeffer, B.A., Loftin, K.A., Werdell, P.J., 2018. Performance metrics for the assessment of satellite data products: an ocean color case study. Opt. Express 26, 7404. https://doi.org/10.1364/OE.26.007404.
Shao, J., 1997. AN ASYMPTOTIC THEORY FOR LINEAR MODEL SELECTION. Stat. Sin. 7, 221–242.
Smith, B., Pahlevan, N., Schalles, J., Ruberg, S., Errera, R., Ma, R., Giardino, C., Bresciani, M., Barbosa, C., Moore, T., Fernandez, V., Alikas, K., Kangro, K., 2021. A chlorophyll-a algorithm for Landsat-8 based on mixture density networks. Front. Remote Sens. 1, 623678 https://doi.org/10.3389/frsen.2020.623678.
Son, Y.-S., Kim, H., 2018. Empirical ocean color algorithms and bio-optical properties of the western coastal waters of Svalbard, Arctic. ISPRS J. Photogramm. Remote Sens. 139, 272–283. https://doi.org/10.1016/j.isprsjprs.2018.03.024.
Stasinopoulos, M.D., Rigby, R.A., Bastiani, F.D., Merder, J., 2022. gamlss.ggplots: Plotting Generalised Additive Model for Location, Scale and Shape. https://CRAN.R-project.org/package=gamlss.ggplots.
Stasinopoulos, D.M., Rigby, R.A., 2007. Generalized additive models for location scale and shape (GAMLSS) in R. J. Stat. Soft. 23 https://doi.org/10.18637/jss.v023.i07.
Stasinopoulos, M.D., Rigby, R.A., Heller, G.Z., Voudouris, V., De Bastiani, F., 2017. Flexible regression and smoothing: using GAMLSS in R. CRC Press/Taylor & Francis Group, Boca Raton.
Steyerberg, E.W., 2018. Validation in prediction research: the waste by data splitting. J. Clin. Epidemiol. 103, 131–133. https://doi.org/10.1016/j.jclinepi.2018.07.010.
Steyerberg, E.W., Harrell, F.E., Borsboom, G.J.J.M., Eijkemans, M.J.C., Vergouwe, Y., Habbema, J.D.F., 2001. Internal validation of predictive models: efficiency of some procedures for logistic regression analysis. J. Clin. Epidemiol. 54, 774–781. https://doi.org/10.1016/S0895-4356(01)00341-9.
Szeto, M., Werdell, P.J., Moore, T.S., Campbell, J.W., 2011. Are the world's oceans optically different? J. Geophys. Res. 116, 2011JC007230 https://doi.org/10.1029/2011JC007230.
Topcu, D., Brockmann, U., 2021. Consistency of thresholds for eutrophication assessments, examples and recommendations. Environ Monit Assess 193, 677. https://doi.org/10.1007/s10661-021-09189-6.
Tzortziou, M., Subramaniam, A., Herman, J.R., Gallegos, C.L., Neale, P.J., Harding, L.W., 2007. Remote sensing reflectance and inherent optical properties in the mid Chesapeake Bay. Estuar. Coast. Shelf Sci. 72, 16–32. https://doi.org/10.1016/j.ecss.2006.09.018.
Valente, A., Sathyendranath, S., Brotas, V., Groom, S., Grant, M., Taberner, M., Antoine, D., Arnone, R., Balch, W.M., Barker, K., Barlow, R., Bélanger, S., Berthon, J.-F., Beşiktepe, Ş., Borsheim, Y., Bracher, A., Brando, V., Canuti, E., Chavez, F., Cianca, A., Claustre, H., Clementson, L., Crout, R., Frouin, R., García-Soto, C., Gibb, S.W., Gould, R., Hooker, S.B., Kahru, M., Kampel, M., Klein, H., Kratzer, S., Kudela, R., Ledesma, J., Loisel, H., Matrai, P., McKee, D., Mitchell, B.G., Moisan, T., Muller-Karger, F., O'Dowd, L., Ondrusek, M., Platt, T., Poulton, A.J., Repecaud, M., Schroeder, T., Smyth, T., Smythe-Wright, D., Sosik, H.M., Twardowski, M., Vellucci, V., Voss, K., Werdell, J., Wernand, M., Wright, S., Zibordi, G., 2019. A compilation of global bio-optical in situ data for ocean-colour satellite applications – version two. Earth Syst. Sci. Data 11, 1037–1068. https://doi.org/10.5194/essd-11-1037-2019.
van Buuren, S., Fredriks, M., 2001. Worm plot: a simple diagnostic device for modelling growth reference curves. Statist. Med. 20, 1259–1277. https://doi.org/10.1002/sim.746.
Volk, T., Hoffert, M.I., 1985. Ocean carbon pumps: Analysis of relative strengths and efficiencies in ocean-driven atmospheric CO2 changes. The carbon cycle and atmospheric CO2: natural variations Archean to present 32, 99–110.
Volpe, G., Santoleri, R., Vellucci, V., Ribera d'Alcalà, M., Marullo, S., D'Ortenzio, F., 2007. The colour of the Mediterranean Sea: global versus regional bio-optical algorithms evaluation and implication for satellite chlorophyll estimates. Remote Sens. Environ. 107, 625–638. https://doi.org/10.1016/j.rse.2006.10.017.
Werdell, P.J., Bailey, S.W., Franz, B.A., Harding Jr., L.W., Feldman, G.C., McClain, C.R., 2009. Regional and seasonal variability of chlorophyll-a in Chesapeake Bay as observed by SeaWiFS and MODIS-aqua. Remote Sens. Environ. 113, 1319–1330. https://doi.org/10.1016/j.rse.2009.02.012.
Werdell, P.J., McKinna, L.I.W., Boss, E., Ackleson, S.G., Craig, S.E., Gregg, W.W., Lee, Z., Maritorena, S., Roesler, C.S., Rousseaux, C.S., Stramski, D., Sullivan, J.M., Twardowski, M.S., Tzortziou, M., Zhang, X., 2018. An overview of approaches and challenges for retrieving marine inherent optical properties from ocean color remote sensing. Prog. Oceanogr. 160, 186–212. https://doi.org/10.1016/j.pocean.2018.01.001.
Werther, M., Odermatt, D., Simis, S.G.H., Gurlin, D., Lehmann, M.K., Kutser, T., Gupana, R., Varley, A., Hunter, P.D., Tyler, A.N., Spyrakos, E., 2022a. A bayesian approach for remote sensing of chlorophyll-a and associated retrieval uncertainty in oligotrophic and mesotrophic lakes. Remote Sens. Environ. 283, 113295 https://doi.org/10.1016/j.rse.2022.113295.
Werther, M., Odermatt, D., Simis, S.G.H., Gurlin, D., Jorge, D.S.F., Loisel, H., Hunter, P. D., Tyler, A.N., Spyrakos, E., 2022b. Characterising retrieval uncertainty of chlorophyll-a algorithms in oligotrophic and mesotrophic lakes and reservoirs. ISPRS J. Photogramm. Remote Sens. 190, 279–300. https://doi.org/10.1016/j.isprsjprs.2022.06.015.
Williams, M., Longstaff, B., Buchanan, C., Llansó, R., Dennison, W., 2009. Development and evaluation of a spatially-explicit index of Chesapeake Bay health. Mar. Pollut. Bull. 59, 14–25. https://doi.org/10.1016/j.marpolbul.2008.11.018.
Wynne, T.T., Tomlinson, M.C., Briggs, T.O., Mishra, S., Meredith, A., Vogel, R.L., Stumpf, R.P., 2022. Evaluating the efficacy of five chlorophyll-a algorithms in chesapeake bay (USA) for operational monitoring and assessment. JMSE 10, 1104. https://doi.org/10.3390/jmse10081104.
Zeng, C., Xu, H., Fischer, A., 2016. Chlorophyll-a estimation around the Antarctica peninsula using satellite algorithms: hints from field water leaving reflectance. Sensors 16, 2075. https://doi.org/10.3390/s16122075.